RSC Advances

PAPER

View Article Online
View Journal | View Issue

Cite this: *RSC Adv.*, 2026, **16**, 30778

Structure and photoluminescence studies of orange-red emitting $Y_3GaO_6:Sm^{3+}$ nanophosphors for lighting applications

Rinki Jangra,[a] Devender Singh, *[a] Reshu Kajal,[a] Pawan Kumar,[a] Sitender Singh,[a] Sakshi Wadhwa,[a] Varun Kumar,[b] Harish Kumar[c] and Ramesh Kumar[d]

Yttrium gallium oxide, Y_3GaO_6, (YGO) phosphors doped with varying concentrations of Sm^{3+} ions have been synthesized using a solution combustion approach. Various spectroscopic and structural analyses were performed on the prepared phosphors to investigate their structural and optical features. The crystal structures and phase characteristics were calculated *via* X-ray diffraction (XRD). The orthorhombic phases of the considered materials with the $Cmc2_1$ space group were confirmed with the help of Rietveld refinement analysis. The morphological features and elemental composition were thoroughly investigated using field emission-scanning electron microscopy (FE-SEM) and energy-dispersive X-ray (EDX) spectroscopy, respectively. Under 406 nm excitation, all Sm^{3+}-doped YGO samples exhibited strong orange emission at 610 nm due to the $^4G_{5/2} \rightarrow {}^6H_{7/2}$ transition. The decay curves showed bi-exponential behavior, indicating the presence of two types of crystallographic sites in the YGO host. A doping concentration of 3 mol% Sm^{3+} ions was found to be optimal, which produced maximum orange emission. Photoluminescence (PL) observations revealed that dipole–dipole interactions were responsible for the concentration quenching phenomenon. The measured color coordinates for all materials lie in the orange-red region of the CIE triangle, making them suitable for lighting applications.

Received 29th January 2026
Accepted 20th May 2026

DOI: 10.1039/d6ra00790b

rsc.li/rsc-advances

1. Introduction

The world-wide energy crisis and complications triggered by climate change have worsened significantly in recent years. Consequently, traditional fluorescent and incandescent lamps have been successfully replaced by white-light-emitting diodes (WLEDs) on account of their prominent benefits, such as longer operational lifetime, high luminous efficiency, improved environmental protection, enhanced optical performance, and many other advantages.[1–4] Currently, commercial WLEDs are manufactured using blue chips coated with Ce^{3+}:YAG (a yellow phosphor) to generate white light. However, the light released by this mixture has a high correlated color temperature (CCT) and low color rendering index (CRI).[5–7] To avoid these limitations, tri-color (red, green, blue or RGB) phosphors are used to generate white light, but this method also suffers from numerous limitations, such as glow inefficiency, color ratio adjustment and re-absorption of light. Thus, commercial WLEDs are inadequate due to the lack of a suitable red component.[8–10] Therefore, there is an urgent need for a stable red-emissive phosphor synthesized using an eco-friendly and low-cost approach for WLED applications.[11,12]

In most cases, phosphors doped with Eu^{3+} are ideal red components for WLEDs, but new orange-red emitters are needed due to the high cost of europium materials.[13] There is an increasing demand for innovative phosphors for applications in the solid-state lighting (SSL) field, particularly luminous materials, for instance rare-earth doped phosphors. The f → f and f → d transitions of rare-earth ions provide sharp and wide emissions, respectively, making them vital in the lighting and display fields.[14,15] Rare-earth doped phosphor materials with red or orange-red emission have been studied for WLEDs. Among the various rare earth metal ions, the Sm^{3+} ion is considered one of the most effective and popular activators for orangish-red emission due to its applications in plasma display panels, lasers, color displays and SSL. The distinctive emission of Sm^{3+} originates from the $^4G_{5/2} \rightarrow {}^6H_J$ (J = 5/2, 7/2, 9/2, and 11/2) transitions.[16–18] Specifically, the $^4G_{5/2} \rightarrow {}^6H_{5/2}$ transition, which produces yellow light, is a magnetic dipole transition, whereas the $^4G_{5/2} \rightarrow {}^6H_{9/2}$ transition, which produces red light, is an electric dipole transition.[19,20] Besides the activator, the choice of host matrix is important because the PL characteristics of the dopant ion are affected by the host. Of the various host lattices reported

[a]*Department of Chemistry, Maharshi Dayanand University, Rohtak-124001, India. E-mail: devjakhar@gmail.com*
[b]*Department of Computer Science and Engineering, University Institute of Engineering and Technology (UIET), Maharshi Dayanand University, Rohtak-124001, India*
[c]*Department of Chemistry, School of Chemical Sciences, Central University of Haryana, Mahendergarh-123031, India*
[d]*Department of Chemistry, Kurukshetra University, Kurukshetra-136119, Haryana, India*

previously, the gallate host matrices are regarded as the best choice for the considered work owing to their chemical stability and tendency to incorporate many rare earth ions.[21,22] Several recent studies have focused on Sm^{3+}-activated gallate-based oxide phosphors, demonstrating their potential as efficient orange-red-emitting materials. Peng *et al.* synthesized a novel $BaLaGaO_4$:Sm^{3+} phosphor exhibiting strong orange-red emission at ~600 nm under 405 nm excitation with excellent thermal stability. The phosphor, when incorporated into a WLED, achieved a high color rendering index and a suitable correlated color temperature. These results demonstrate that $BaLaGaO_4$:Sm^{3+} is a promising orange-red emitting material for indoor lighting and anti-counterfeiting applications.[23] Moreover, Govindan *et al.* synthesized Sm^{3+}-activated $Ca_3Ga_4O_9$ (CGO:Sm^{3+}) phosphors *via* a solid-state reaction, exhibiting intense orange-red emission. The phosphor showed favorable optical and photometric properties, including CIE chromaticity coordinates in the orange-red region, high color purity, and a suitable correlated color temperature, making it highly suitable for LED applications.[24] Additionally, there are several methods for synthesizing inorganic phosphor materials, such as sol–gel, solution combustion, solid-state, hydrothermal, co-precipitation, and many others. The solution combustion technique was chosen for the synthesis of nanomaterials because of its ability to produce homogeneous and high-purity nanoparticles, its low processing temperature, and decreased synthesis time.[25,26]

In this work, a series of Y_3GaO_6 phosphors doped with Sm^{3+}, having good homogeneity, nanoparticle size dispersion, and high purity, was synthesized using a gel combustion approach. The obtained samples were analyzed in detail using several methods to get information about different properties. XRD, EDX, Rietveld refinement, and FE-SEM analyses were carried out to investigate their structural and morphological characteristics. The PL characteristics (excitation and emission spectra, concentration quenching mechanism, and energy transfer mechanism) were thoroughly investigated to evaluate the luminescence performance of the synthesized samples. The results obtained for the synthesized Y_3GaO_6:Sm^{3+} phosphors revealed their suitability for lighting applications.

2. Experimental procedure

A series of Sm^{3+}-doped Y_3GaO_6 phosphors has been synthesized using the combustion technique. The raw materials for this synthesis include high-purity yttrium nitrate hexahydrate, gallium nitrate hydrate, samarium nitrate hexahydrate, and urea, obtained from Sigma-Aldrich. The amounts of these materials were calculated and weighed accurately. Initially, the weighed chemicals, *viz.* $Y(NO_3)_3 \cdot 6H_2O$, $Sm(NO_3)_3 \cdot 6H_2O$, and $Ga(NO_3)_3 \cdot xH_2O$ were mixed in de-ionized water in a beaker to attain a homogeneous solution. The beaker was placed on a magnetic stirrer and the solution was stirred continuously at 80 °C for 25–30 minutes to form a viscous solution. Then, urea was added with some double-distilled water and stirring was continued until a gel-like substance was formed. The formed substance was transferred into a crucible and positioned in a muffle furnace pre-heated to 600 °C for about 15 minutes. Within a few minutes, an exothermic combustion process began, resulting in a white fluffy powder and the evolution of gaseous products (CO_2, N_2O, *etc*). The obtained material was

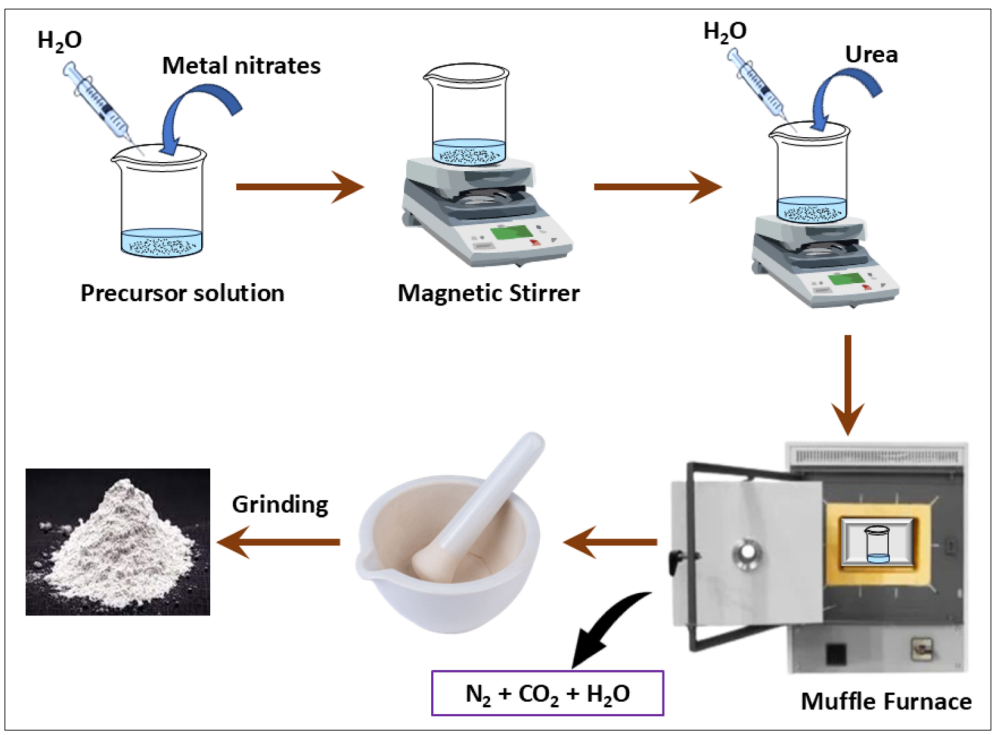

Fig. 1 Schematic of the various steps involved in the solution combustion synthesis.

cooled and crushed in an agate mortar to get a fine powder. The synthesized powder was transferred to an alumina crucible and calcined at 1300 °C for 5 hours to obtain the desired phase.[27–30] The calcination temperature of 1300 °C for 5 hours was selected based on preliminary synthesis and XRD characterization of prepared samples. The sample was synthesized at 600 °C and further calcined at various temperatures, *i.e.*, 800, 1000, 1100, 1200 and 1300 °C. At lower calcination temperatures, secondary phases and incomplete crystallization were observed in the XRD patterns.[31,32] The overall representation of the solution combustion synthetic procedure is depicted in Fig. 1.

3. Characterizations

The synthesized compounds were characterized using several spectroscopic techniques to reveal their characteristics. Powder XRD patterns of the as-prepared materials were obtained on a Rigaku Ultima X-ray diffractometer using Cu-Kα radiations with a 2θ scanning step equal to 0.02°. The refined variables of the crystal structures of the host and optimized samples were determined using Rietveld analysis. The morphology of the samples was investigated in detail *via* FE-SEM, on a Carl Zeiss Sigma 360 instrument. EDX measurements and elemental mapping were conducted using an Ametek energy-dispersive X-ray spectrometer. PL spectra were obtained on a Horiba Jobin-Yvon Fluorolog-3 spectrophotometer at room temperature with a Xe lamp as the excitation source.

4. Results and interpretation

4.1 Phase and structural investigation

The XRD patterns of the host and all Sm^{3+}-doped Y_3GaO_6 samples with varying concentrations were obtained to examine the crystal framework and phase purity of the synthesized samples. The XRD patterns obtained for these samples in the $2\theta = 10–65°$ range are specified in Fig. 2(a), and it was found that all diffraction peaks matched closely with standard XRD data corresponding to JCPDS Card No. 53-1225, which confirmed the orthorhombic structure of the considered nanomaterials with the $Cmc2_1$ space group.[33] No impurity peaks were present in the lattice, even after the incorporation of Sm^{3+} ions, validating the preparation of pure and single-phase samples using the solution combustion technique. This confirmed the efficient replacement of Y^{3+} ions by Sm^{3+} ions in the host structure, and that doping with Sm^{3+} ions did not induce any notable change in the Y_3GaO_6 host assembly. The similarity in ionic radius between Sm^{3+} (1.02 Å) and Y^{3+} (0.96 Å), as compared with the smaller radius of Ga^{3+} (0.47 Å), facilitates the effective substitution of Y^{3+} by Sm^{3+} within the host matrix. This substitution resulted in a noticeable shift of diffraction peaks to lower 2θ values with increasing Sm^{3+} content, as depicted in Fig. 2(b). The observed shift indicates the expansion of the crystal lattice as a result of the replacement of smaller Y^{3+} ions with larger Sm^{3+} ions. The interplanar *d*-spacing corresponding to the peak with the highest intensity was calculated for each composition using Bragg's law, given in eqn (1) (ref. 34) as follows:

$$2d\sin\theta = n\lambda \quad (1)$$

Table 1 summarizes the calculated *d*-spacing values along with their respective 2θ positions. Based on earlier studies, a radius percentage difference (D_d) of less than 30% between the host and dopant ions is generally acceptable for effective substitution. This difference is calculated using the expression provided in eqn (2) (ref. 35) as follows:

$$D_d = \left|\frac{R_s(CN) - R_d(CN)}{R_s(CN)}\right| \times 100\% \quad (2)$$

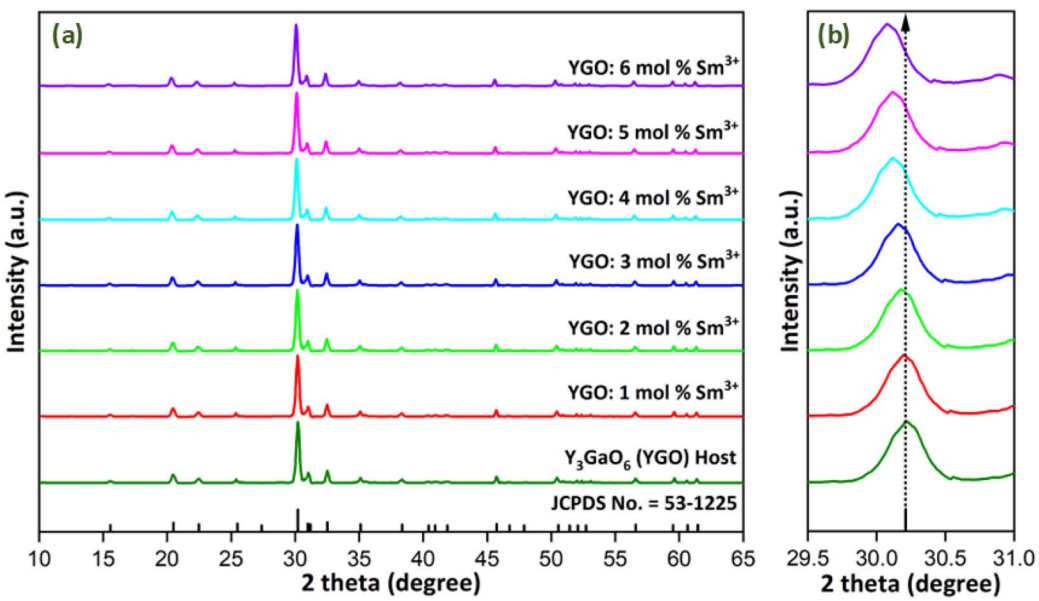

Fig. 2 (a) XRD patterns of the host and Sm^{3+}-doped YGO samples with standard JCPDS data. (b) Enlarged view of the most intense diffraction peaks.

Table 1 Interplanar d-spacing values for the host and Sm^{3+}-doped YGO phosphors

YGO:x mol% Sm^{3+}	2θ (°)	d-spacing (Å)
YGO host	30.2207	2.9550
YGO:1 mol% Sm^{3+}	30.1962	2.9573
YGO:2 mol% Sm^{3+}	30.1813	2.9587
YGO:3 mol% Sm^{3+}	30.1600	2.9608
YGO:4 mol% Sm^{3+}	30.1174	2.9649
YGO:5 mol% Sm^{3+}	30.1036	2.9663
YGO:6 mol% Sm^{3+}	30.0812	2.9684

In the given relation, CN stands for coordination number, while R_s and R_d correspond to the ionic radii of the host and dopant ion, respectively. The calculated value of D_d being below 30% confirmed the effective substitution of Sm^{3+} ions into the host lattice. Additionally, the average crystallite size (D) of the synthesized powder samples was estimated using the Debye–Scherrer formula, expressed in eqn (3) (ref. 36) as follows:

$$D = \frac{k\lambda}{\beta \cos \theta} \quad (3)$$

In this context, λ denotes the incident X-ray wavelength (1.5406 Å), k refers to the shape factor or Scherrer constant (commonly taken as 0.9), θ is the angle of diffraction, and β signifies peak broadening expressed in radians. To analyze matrix strain (ε) and crystallite size (D), the Williamson–Hall (W–H) method was used, based on the relation given in eqn (4), and the calculated

Table 2 Crystallite sizes obtained from the Debye–Scherrer and W–H methods, along with the microstrain values for the YGO host and YGO:$x$$Sm^{3+}$ (x = 1–6 mol%) phosphors

YGO:x mol% Sm^{3+}	2θ (°)	FWHM (radians)	Crystallite size, D (nm)		Microstrain, $\varepsilon \times 10^{-3}$
			D_{SC}	D_{W-H}	
YGO host	30.2207	0.30713	27.98	45.64	4.96
YGO:1 mol% Sm^{3+}	30.1962	0.29683	28.95	46.38	4.80
YGO:2 mol% Sm^{3+}	30.1813	0.28321	30.34	48.92	4.58
YGO:3 mol% Sm^{3+}	30.1600	0.31572	27.22	45.71	5.11
YGO:4 mol% Sm^{3+}	30.1174	0.29543	29.08	47.86	4.79
YGO:5 mol% Sm^{3+}	30.1249	0.28125	30.55	48.24	4.56
YGO:6 mol% Sm^{3+}	30.0812	0.32493	26.44	44.15	5.28

crystallite size was compared with the data obtained from the W–H plots[37] as follows:

$$\beta = \frac{K\lambda}{D \cos \theta} + 4\varepsilon \tan \theta \quad (4)$$

This equation can be rearranged to obtain eqn (5) as follows:[38]

$$\beta \cos \theta = \frac{K\lambda}{D} + 4\varepsilon \sin \theta \quad (5)$$

The W–H equation represents a linear relation where plotting 4 sinθ *versus* β cosθ yields a straight line with slope ε and y-intercept $K\lambda/D$. The slope represents microstrain (ε), and the y-

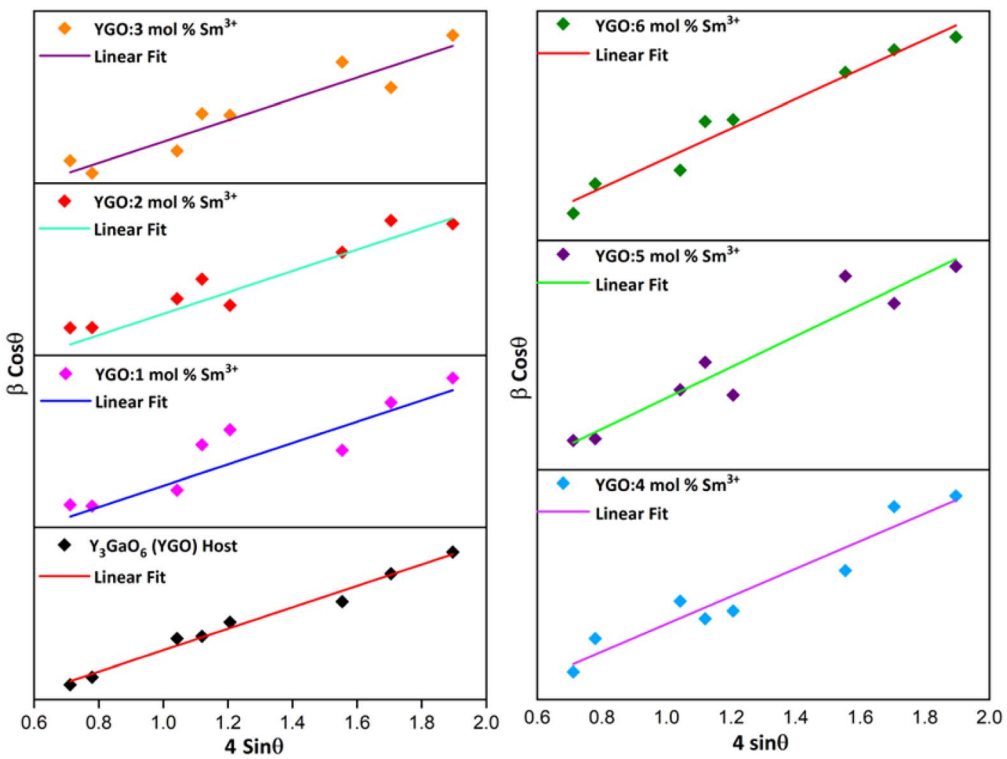

Fig. 3 W–H graphs of the host and all Sm^{3+}-doped YGO nanophosphors.

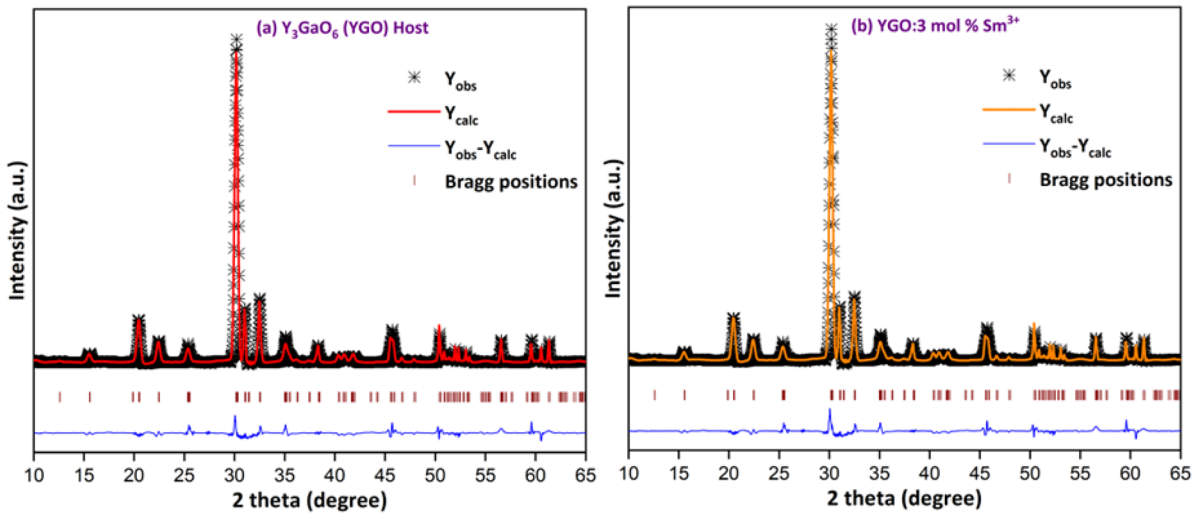

Fig. 4 Rietveld images of the (a) host and (b) optimized samples, representing the observed (×lines) and calculated data (solid lines).

Table 3 Refined parameters for the host and optimized samples obtained from Rietveld analysis

Sample parameters	Y_3GaO_6	$Y_{2.97}GaO_6$:3 mol% Sm^{3+}
Molecular weight (M)	432.45 g mol^{-1}	434.29 g mol^{-1}
Crystal system/symmetry	Orthorhombic	Orthorhombic
Lattice symbol	oC	oC
Space group (H–M)	$Cmc2_1$	$Cmc2_1$
Bravais lattice	C	C
Formula unit (Z)	4	4
Hall symbol	C2c-2	C2c-2
Laue class	mmm	mmm
Point group	mm2	mm2
Space group number	36	36
Centrosymmetric	Acentric	Acentric
$\alpha = \beta = \gamma$	90°	90°
a (Å)	8.88750	8.93895
b (Å)	11.15120	11.35714
c (Å)	5.42170	5.52586
Volume (Å^3)	537.3245	560.9903
R_p (%)	4.3521	4.5982
R_{wp} (%)	5.1622	5.8643
χ^2 (%)	2.342	2.675
Density, ρ (g cm^{-3})	5.34	5.14
θ range (°)	10°–65°	10°–65°

intercept ($K\lambda/D$) allows the calculation of the crystallite size (D). Fig. 3 illustrates W–H plots for both undoped and Sm^{3+}-doped Y_3GaO_6 nanomaterials. The results revealed that the crystallite sizes estimated *via* the W–H method are generally larger than those obtained from the Scherrer equation, probably due to the inclusion of strain effects in the W–H method. A comparison of results from both methods, along with microstrain values, is given in Table 2.

4.2 Rietveld structural refinement

Rietveld refinement analysis was conducted using the FULLPROF program to investigate the crystal structures of both the host and the optimized samarium-doped sample. Fig. 4 displays the observed diffraction patterns together with the fitted data for the host and doped sample. In the figure, experimental points are indicated by black crosses, the calculated profile for the host is shown as a solid dark red line, and that for the optimized sample is represented as a solid orange line. The difference between the observed and calculated intensities is plotted as a blue curve at the bottom of the figure with vertical lines marking Bragg reflection positions. The refined crystallographic parameters for both the host and optimized samples are listed in Table 3, confirming that the synthesized materials crystallize in an orthorhombic structure with space group $Cmc2_1$. Each unit cell of Y_3GaO_6 contains four formula units comprising 12 yttrium, 4 gallium and 24 oxygen atoms. The atomic positions, symmetry operations, Wyckoff sites and occupancy details are presented in Table 4. In the YGO lattice, each Y^{3+} ion is coordinated by seven O-atoms, creating a distorted YO_7 dodecahedron, whereas each Ga^{3+} ion is coordinated by four O-atoms, creating a GaO_4 tetrahedron. Fig. 5 illustrates the structure of the host lattice and the coordination environment of Y and Ga atoms with oxygen. The refinement variables $R_p = 4.3521\%$, $R_{wp} = 5.1622\%$, and $\chi^2 = 2.342$ for the host, and $R_p = 4.5982\%$, $R_{wp} = 5.8643\%$ and $\chi^2 = 2.675$ for the 3 mol% Sm^{3+}-doped sample demonstrate the accuracy of refinement and the successful synthesis of a high-purity material. As shown in Table 3, the lattice parameters of the samarium-doped sample are slightly larger than those of the

Table 4 Atomic parameters corresponding to different atoms present in the lattice

Atom	x	y	z	Site	Occupancy	Symmetry
Y1	0.19307	0.10564	0.46692	8b	1.000	1
Y2	0.00000	0.39591	0.42384	4a	1.000	m
Ga1	0.00000	0.19261	0.00000	4a	1.000	m
O1	0.15850	0.26000	0.18600	8b	1.000	1
O2	0.33720	0.01390	0.20800	8b	1.000	1
O3	0.00000	0.05000	0.13300	4a	1.000	m
O4	0.00000	0.21380	0.67800	4a	1.000	m

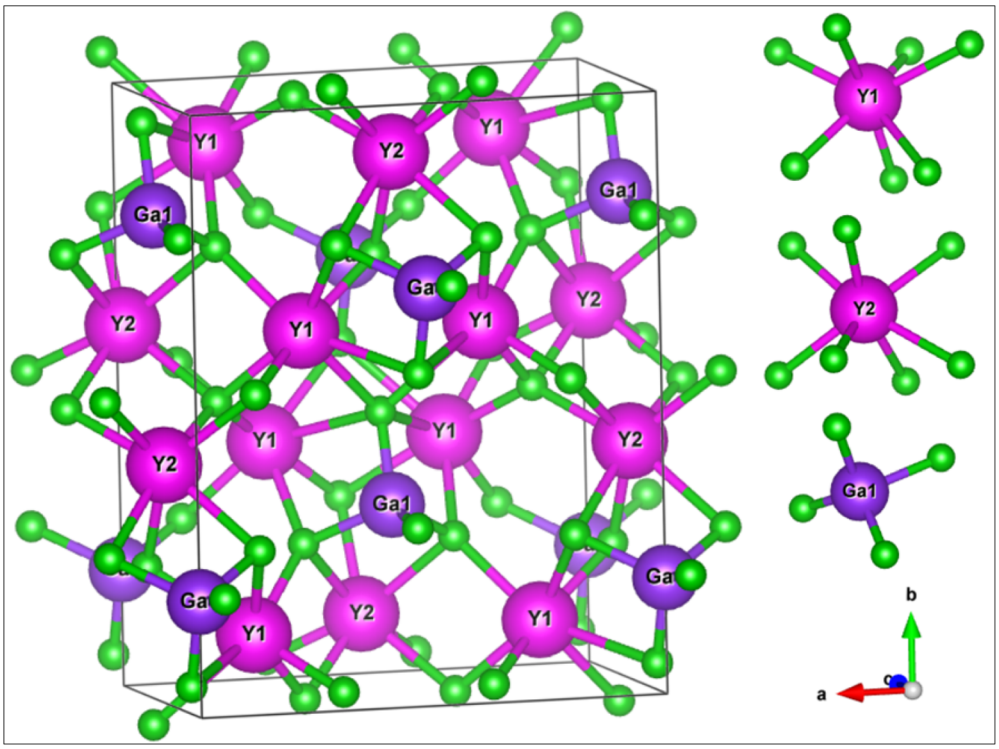

Fig. 5 Crystal structure of the YGO material showing the coordination of the Y and Ga atoms with their surrounding O atoms.

undoped host, which can be attributed to the replacement of the smaller Y^{3+} ions by the larger Sm^{3+} ions, thereby confirming the effective incorporation of samarium ions into the crystal lattice.

4.3 EDX analysis

To confirm the successful synthesis and elemental composition of the Sm^{3+}-doped Y_3GaO_6 phosphor, EDX spectroscopy was employed. This technique provided both qualitative and quantitative data regarding the presence and distribution of elements within the sample. The EDX spectrum recorded at multiple regions of sample surface exhibited diverse peaks corresponding to yttrium (Y), gallium (Ga), oxygen (O) and samarium (Sm), as demonstrated in Fig. 6. The detection of Sm peaks confirmed the incorporation of dopant ions into the host lattice and the presence of only Y, Ga, O and Sm elements without any additional or unpredicted peaks specified the single phase of the produced material. Furthermore, elemental plots were performed for the optimized sample, and the resulting elemental maps for Y, Ga, O, and Sm are presented in Fig. 7. These images clearly demonstrate the homogeneous distribution of the dopant and host elements, validating the efficient synthesis of the phosphor material. The atomic and weight percentages of fundamental elements in the synthesized phosphor are listed in Table 5.

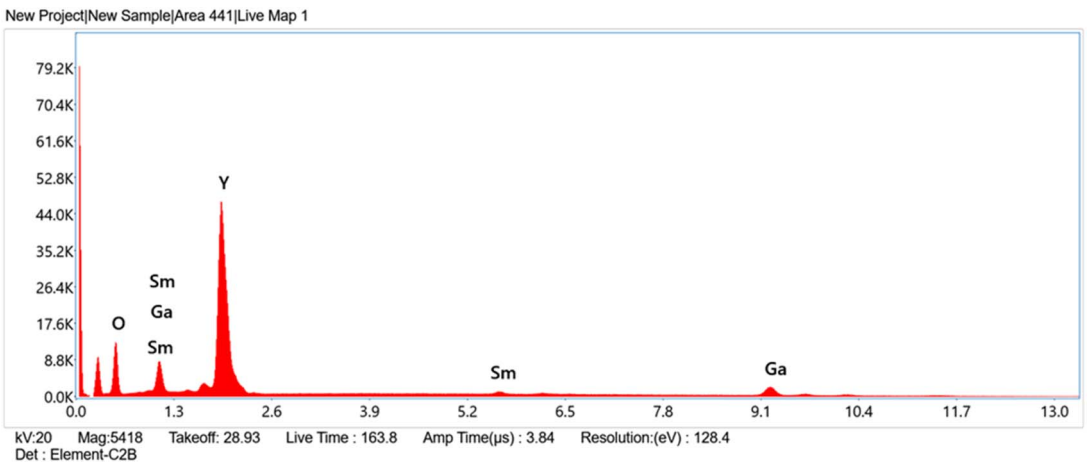

Fig. 6 EDX spectra showing the peaks corresponding to all elements present in the optimized sample.

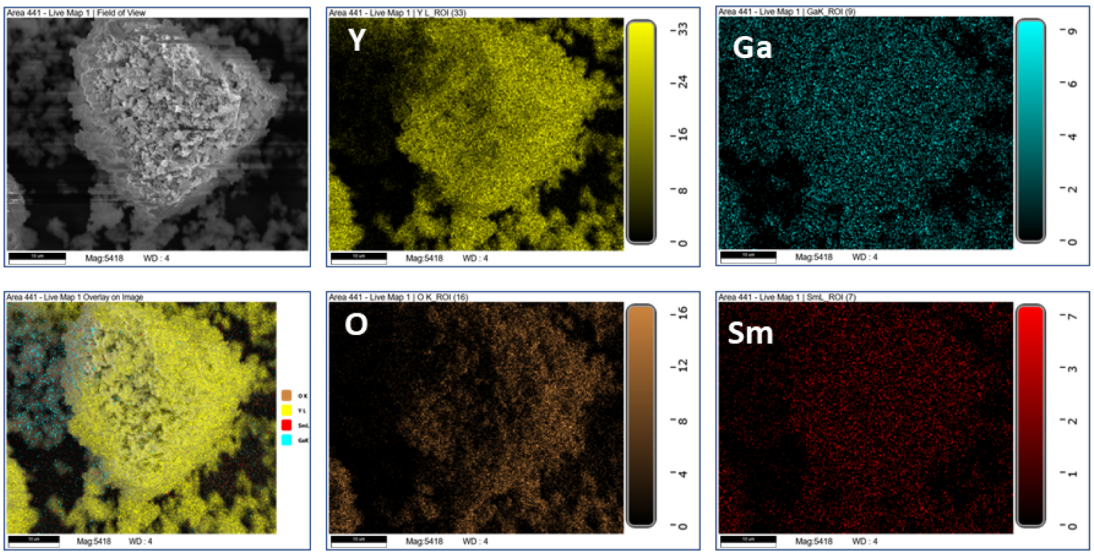

Fig. 7 Elemental mapping images of the optimized sample.

Table 5 Atomic and weight % of various atoms present in the optimized sample

Element	Series	Weight (%)	Atomic (%)
Y (yttrium)	L-series	53.3	20.6
Sm (samarium)	L-series	2.2	0.5
Ga (gallium)	K-series	10.0	4.9
O (oxygen)	K-series	34.5	74.0

4.4 Morphological characteristics

FE-SEM analysis was conducted on the optimized $Y_{2.97}GaO_6$:3-mol% Sm^{3+} phosphor to investigate its surface morphology, including particle shape, structure, and size distribution. The obtained FE-SEM images are presented in Fig. 8(a), indicating that the particles exhibit agglomeration and irregular shapes. The average particle size falls within the 40–60 nm range. Due to their nanometer-scale dimensions, this Sm^{3+}-doped phosphor is suitable for various applications in lighting devices. The gases released during the combustion process and high-temperature heat treatment commonly result in particle agglomeration, owing to small particles clustering *via* diffusion.[39] A histogram showing the particle size distribution in the optimized sample is represented in Fig. 8(b).

4.5 Photoluminescence investigations

4.5.1 Excitation and emission spectra. The photoluminescence excitation (PLE) characteristics of the $Y_{3-x}GaO_6$:xSm^{3+} (x = 3 mol%) phosphors were examined and the resulting spectrum recorded in 200–550 nm range with an emissive wavelength of 600 nm is shown in Fig. 9. The spectrum displays seven excitation peaks located at 349 nm, 365 nm, 377 nm, 406 nm, 422 nm, 440 nm and 464 nm, which correspond to transitions from the $^6H_{5/2}$ ground state to the $^4K_{17/2}$,

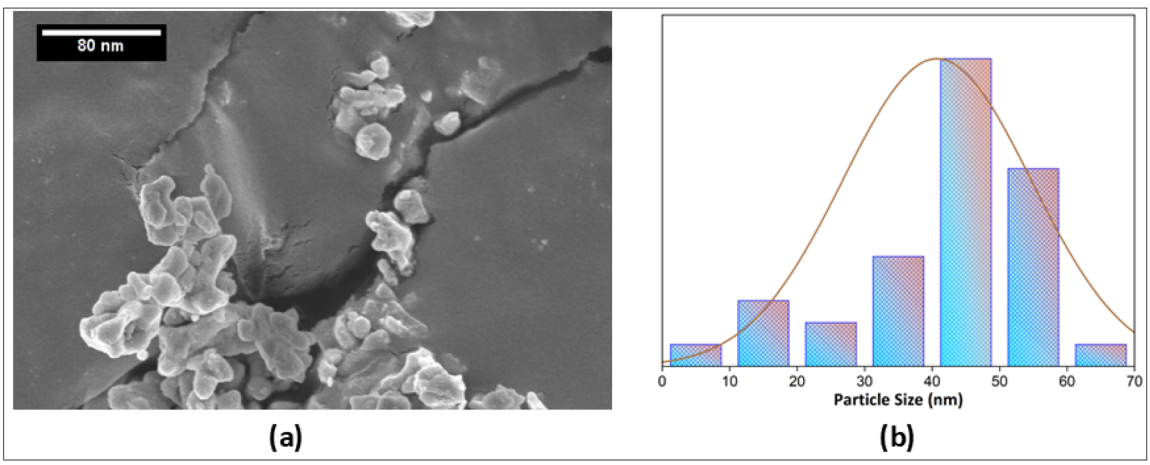

Fig. 8 (a) FE-SEM image of the optimized YGO:3 mol% Sm^{3+} phosphor. (b) Histogram of the particle size distribution.

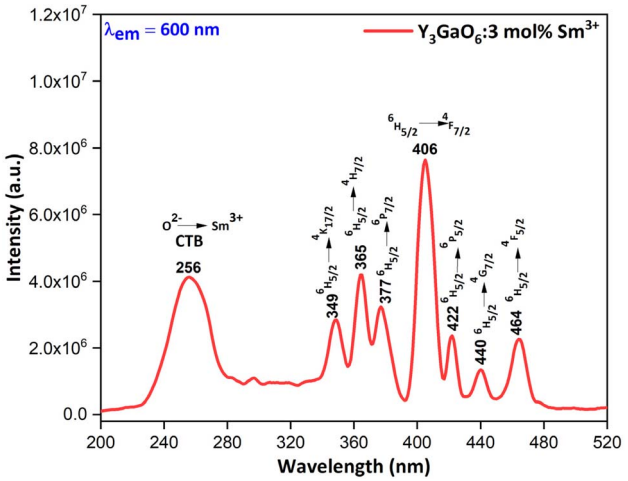

Fig. 9 Excitation spectra of the YGO:Sm^{3+} phosphor with a 3 mol% doping concentration of Sm^{3+} ions.

$^4H_{7/2}$, $^6P_{7/2}$, $^4F_{7/2}$, $^6P_{5/2}$, $^4G_{7/2}$ and $^4F_{5/2}$ excited states of Sm^{3+}, respectively. In addition, a charge-transfer band also appeared at 256 nm owing to the transition from O^{2-} to the Sm^{3+} ion.[40–42] The excitation peak at 406 nm exhibited the strongest intensity and was consequently used to excite the prepared phosphors for emission spectral analysis. Photoluminescence emission (PL) spectra of trivalent samarium-doped YGO nanophosphors with varying Sm^{3+} concentrations (1–6 mol%) were recorded at an excitation wavelength of 406 nm, as displayed in Fig. 10. The obtained PL spectra demonstrated three bands, with the least intense band observed at 568 nm, the most intense band at 610 nm, and a moderately intense band at 653 nm, equivalent to

Table 6 Asymmetry ratio (R) for all Sm^{3+}-doped YGO phosphors with varying concentrations of Sm^{3+} ions

YGO:x mol% Sm^{3+}	$x = 1$	$x = 2$	$x = 3$	$x = 4$	$x = 5$	$x = 6$
R	1.35	1.25	1.60	1.41	1.03	1.15

$^4G_{5/2} \rightarrow {}^6H_{5/2}$, $^6H_{7/2}$ and $^6H_{9/2}$ transitions, respectively.[43,44] The orange-red color of $Y_{3-x}GaO_6$:xSm^{3+} (x = 1–6 mol%) samples is due to the most intense peak at 610 nm arising from the electronic transition $^4G_{5/2} \rightarrow {}^6H_{7/2}$. The transitions $^4G_{5/2} \rightarrow {}^6H_{9/2}$ at 653 nm and $^4G_{5/2} \rightarrow {}^6H_{5/2}$ at 568 nm are electric dipole and magnetic dipole allowed, respectively. The magnetic dipole transitions follow the $\Delta J = 0, \pm 1$ selection rule and are not affected by the environment of the Sm^{3+} ions. On the other hand, electric dipole transitions follow the $\Delta J = 2$, 4 and 6 ($\Delta J \leq 6$) selection rule and are affected by the environment of the Sm^{3+} ions.[45,46]

4.5.2 Asymmetry ratio. The asymmetry ratio (R) may be defined as the ratio of the intensity of the electric dipole transition (I_{ED}) to the intensity of the magnetic dipole transition (I_{MD}) and is expressed in eqn (6) (ref. 47) as follows:

$$R = \frac{I_{ED}}{I_{MD}} \quad (6)$$

This ratio describes the asymmetric or symmetric nature of the local environment of the Sm^{3+} ions in the lattice. The asymmetry around the doped ion in the host lattice is validated by a large value of R ($R > 1$).[48] In the present work, I_{ED} is higher than I_{MD}, which gives an R-value greater than one (Table 6),

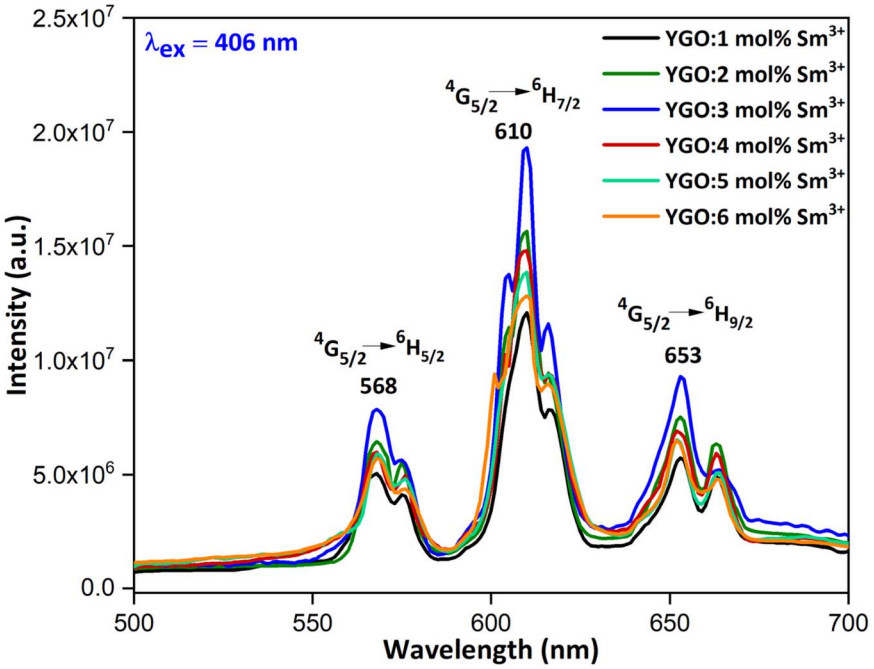

Fig. 10 Emission spectra of the YGO:Sm^{3+} phosphors with varying doping concentrations of Sm^{3+} ions.

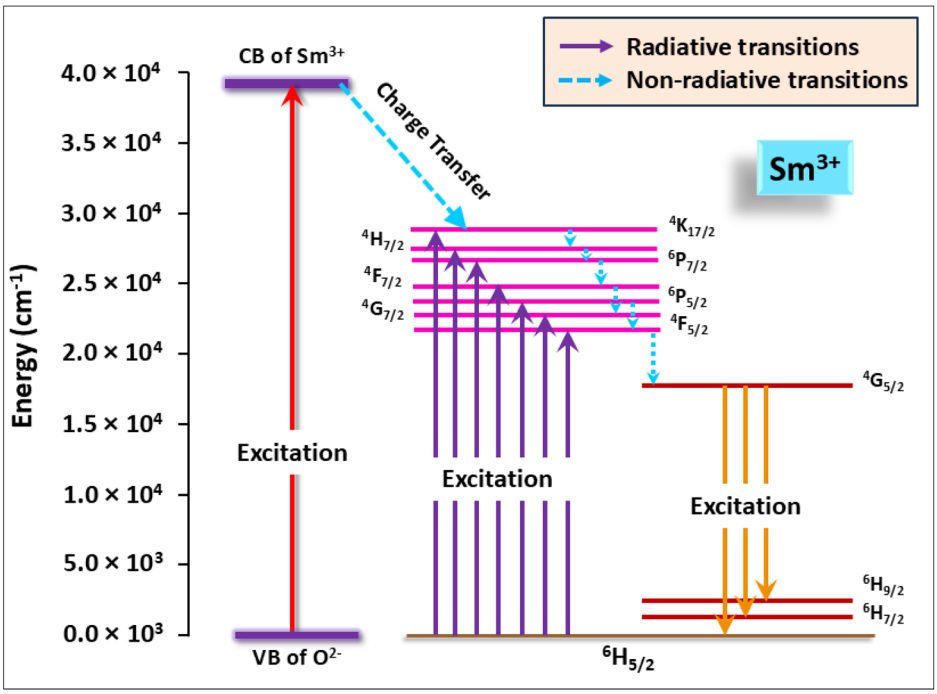

Fig. 11 Energy level diagram representing the radiative and non-radiative transitions of the Sm^{3+} ions in the YGO phosphors.

suggesting that Sm^{3+} ions are located at asymmetric sites in the lattice. Fig. 11 presents an energy level illustration of Sm^{3+}-doped YGO nanophosphors, demonstrating radiative and non-radiative transitions. All excited states above $^4G_{5/2}$ rapidly relax non-radiatively to this state, attributed to minimal energy gaps between these states. Radiative relaxation from the $^4G_{5/2}$ level to

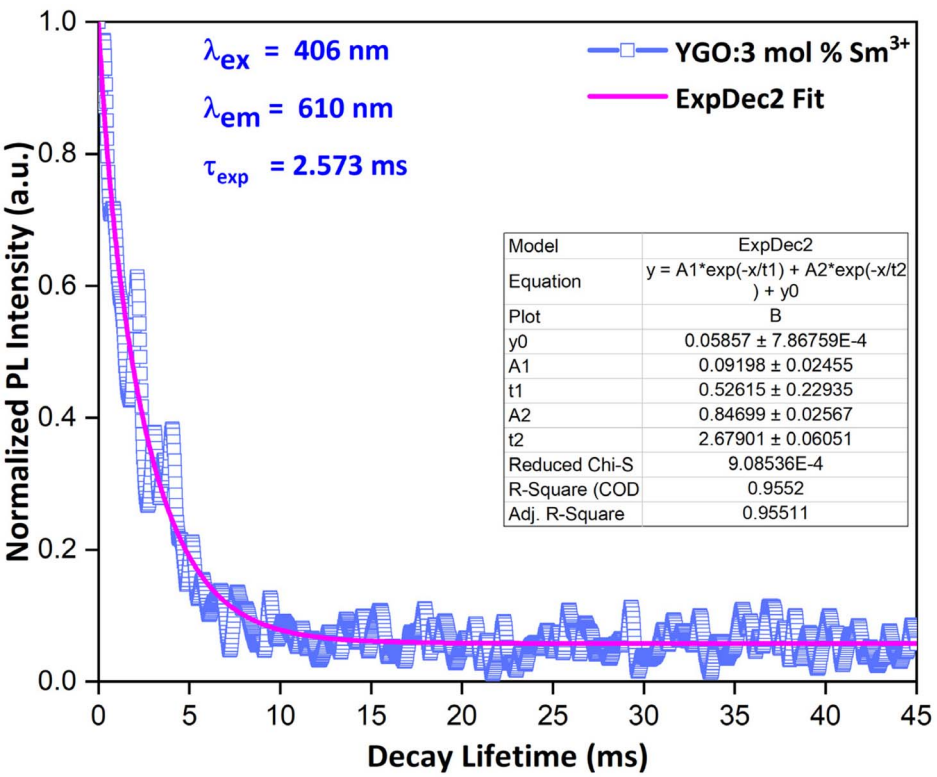

Model	ExpDec2
Equation	y = A1*exp(-x/t1) + A2*exp(-x/t2) + y0
Plot	B
y0	0.05857 ± 7.86759E-4
A1	0.09198 ± 0.02455
t1	0.52615 ± 0.22935
A2	0.84699 ± 0.02567
t2	2.67901 ± 0.06051
Reduced Chi-S	9.08536E-4
R-Square (COD	0.9552
Adj. R-Square	0.95511

Fig. 12 Decay lifetime curve of the YGO:3 mol% Sm^{3+} phosphor.

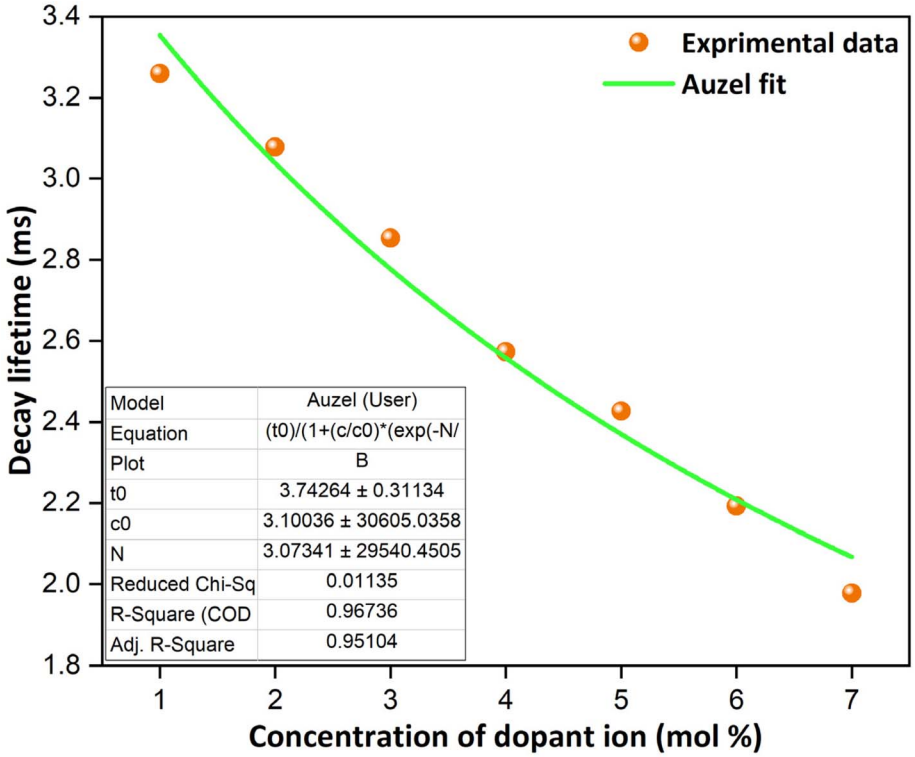

Fig. 13 Variation of lifetime with the dopant ion concentration.

Table 7 Experimental lifetime and quantum efficiency values of the synthesized $Y_{3-x}GaO_6$:xSm^{3+} (x = 1–6 mol%) nanophosphors

Sample	τ_{exp} (ms)	η (%)
YGO:1 mol% Sm^{3+}	3.259	87.08
YGO:2 mol% Sm^{3+}	3.078	82.24
YGO:3 mol% Sm^{3+}	2.854	76.25
YGO:4 mol% Sm^{3+}	2.573	68.75
YGO:5 mol% Sm^{3+}	2.427	64.85
YGO:6 mol% Sm^{3+}	2.192	58.57
YGO:7 mol% Sm^{3+}	1.978	52.85

the lower $^6H_{5/2}$, $^6H_{7/2}$ and $^6H_{9/2}$ states occurs on account of significant energy differences between these states.

4.5.3 Lifetime measurements. The analysis of luminescence decay lifetimes serves as an important parameter for understanding emission properties, quenching mechanisms and energy transfer behavior. The luminescence decay curve recorded by monitoring excitation at 406 nm and emission at 610 nm for the $Y_{2.97}GaO_6$:3 mol% Sm^{3+} nanophosphor is shown in Fig. 12. The decay profile exhibits bi-exponential behavior for the optimized sample and the experimental lifetime value was calculated using the expression presented in eqn (7) (ref. 49) as follows:

$$I_t = I_0 + A_1\exp\left(-\frac{t}{\tau_1}\right) + A_2\exp\left(-\frac{t}{\tau_2}\right), \quad (7)$$

where I_t and I_0 are the emission intensities at time $t = t$ and at $t = 0$, respectively. τ_1 and τ_2 are fast and slow decay components, respectively, while the coefficients A_1 and A_2 are residual fitting parameters. The experimental lifetime (τ_{exp}) values of the phosphor demonstrating non-exponential behavior can be obtained using eqn (8) (ref. 50) as follows:

$$\tau_{exp} = \frac{A_1\tau_1^2 + A_2\tau_2^2}{A_1\tau_1 + A_2\tau_2} \quad (8)$$

Fig. 13 displays the variation of the observed lifetime in the Y_3GaO_6 lattice with the changes in concentration of Sm^{3+} ion using Auzel's fitting function. A linear decrease in the value of the experimental lifetime (τ_{exp}) from 3.259 ms to 1.978 ms was observed on increasing the concentration of Sm^{3+} ions from 1 to 6 mol%, as shown in Table 7. As the concentration of the dopant Sm^{3+} ion increased, the separation between ions decreased, leading to a greater probability of non-radiative energy transfer, and the lifetime decreased; this phenomenon is known as luminescence quenching. Auzel's model, given in eqn (9), also describes the dependence of lifetime values on the concentration of the dopant ion[51] as follows:

$$\tau_c = \frac{\tau_0}{1 + \frac{C}{C_0}e^{-N/3}} \quad (9)$$

In this expression, τ_c and τ_0 denote the measured lifetime and the intrinsic radiative lifetime, respectively. The parameter C denotes the concentration of the Sm^{3+} ions, while C_0 is a constant and N signifies the number of phonons generated during the relaxation process. For the $Y_{2.97}GaO_6$:3 mol% Sm^{3+} nanophosphor, the fitting of experimental data to Auzel's model

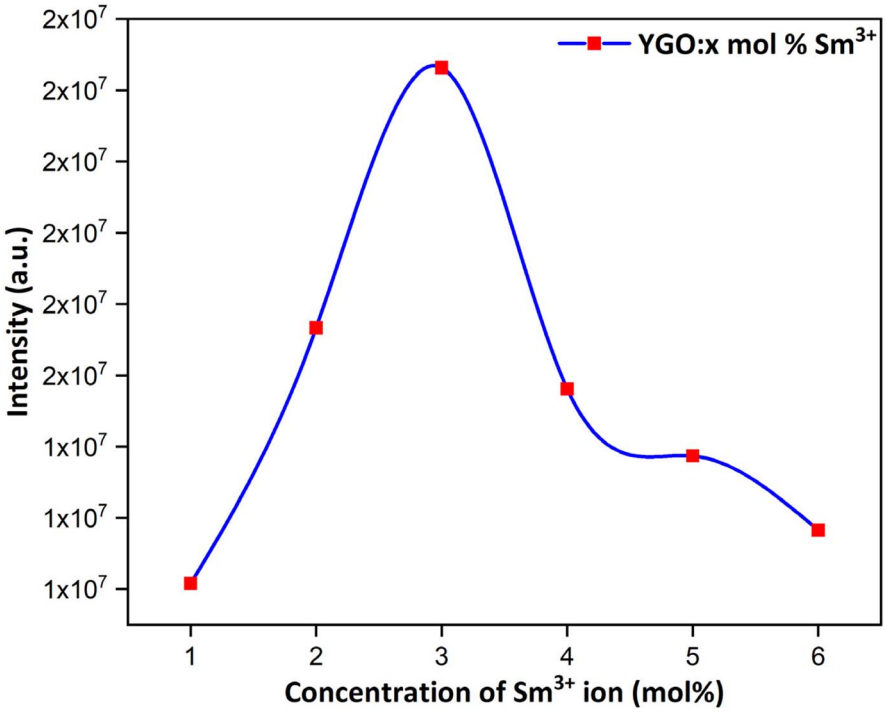

Fig. 14 Effect of the concentration of Sm^{3+} ions on the emission intensity of the samples.

gives a radiative lifetime (τ_o) of 3.74264 ms, as displayed in Fig. 13. The ratio of the experimental decay lifetime (τ_{exp}) to the radiative lifetime (τ_o) is defined as the luminous quantum efficiency (η) of the rare-earth-doped materials and can be calculated using eqn (10) (ref. 52) as follows:

$$\eta = \frac{\tau_{exp}}{\tau_0} \times 100\% \quad (10)$$

The resulting quantum efficiency values of all the doped samples are summarized in Table 7. The high quantum

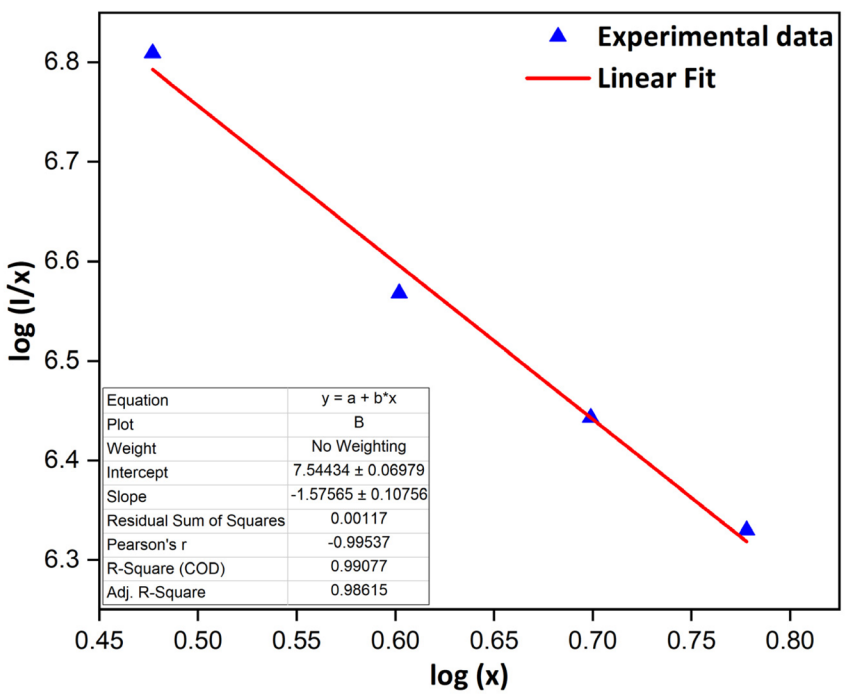

Fig. 15 Relationship of log(1/x) *vs.* log(x) in the $Y_{3-x}GaO_6$:xSm^{3+} (x = 1–6 mol%) phosphors.

efficiency obtained from the synthesized nanomaterials makes these materials suitable for incorporation into white light-emitting diodes for lighting purposes.

4.5.4 Concentration quenching. The increasing content of doped Sm^{3+} ions increases the luminous intensity, which is maximum at the Sm^{3+} ion concentration of 3 mol%, and then declines continuously owing to concentration quenching, as shown in Fig. 14. The concentration quenching is generally observed in rare-earth doped phosphors as the amount of dopant increases. The increasing Sm^{3+} content shortens the distance between doped samarium ions, which results in more non-radiative energy transfer among activators, instead of radiative energy transfer. The increase in the probability of non-radiative energy transfer among luminescent centers is the cause of luminescence quenching. Non-radiative energy transfer generally occurs through exchange interactions, radiative reabsorption, or multipole interactions.[53,54] Radiative reabsorption takes place only if there is considerable overlap between excitation and emission spectra, which is absent in the prepared phosphors. The critical distance refers to the separation between Sm^{3+} ions at the critical concentration (x_c), beyond which the luminous intensity begins to decline and can be determined by eqn (11) (ref. 55) as follows:

$$R_c = 2\left(\frac{3V}{4\pi x_c Z}\right)^{1/3} \quad (11)$$

where V and Z denote the volume of the unit cell and the number of lattice sites per unit cell that can be occupied by an activator ion. The critical distance for an effective exchange interaction is approximately 5 Å, beyond which the strength of the interaction weakens. Taking experimental values of x_c, V, and Z ($x_c = 0.03$, $V = 560.9903$ Å^3, and $Z = 4$), R_c was calculated to be 20.7490 Å, which was greater than 5 Å, and specified that the energy transfer mechanism is governed by multipolar interactions. Multipolar interactions are classified into three types: dipole–dipole (d–d), dipole–quadrupole (d–q) and quadrupole–quadrupole (q–q) interactions. The particular type of multipolar interaction can be determined by analyzing the variation of the emission intensity with activator ion concentration beyond the critical concentration. Van Uitert's model describes the relationship between emission intensity (I) and activator concentration (x), as described in eqn (12) (ref. 56 and 57) as follows:

$$\frac{I}{x} = \frac{K}{1 + \beta(x)^{\frac{M}{3}}} \quad (12)$$

For simplification, it can be rewritten in the form given in eqn (13) (ref. 58) as follows:

$$\log\left(\frac{I}{x}\right) = -\frac{M}{3}\log(x) + k' \quad (13)$$

where $k' = \log K - \log \beta$, whereas I signifies radiative intensity, x denotes the activator ion doping concentration, and M symbolizes the multipolar interaction index, with values equal to 6, 8, and 10, consistent with d–d, d–q, and q–q interactions,

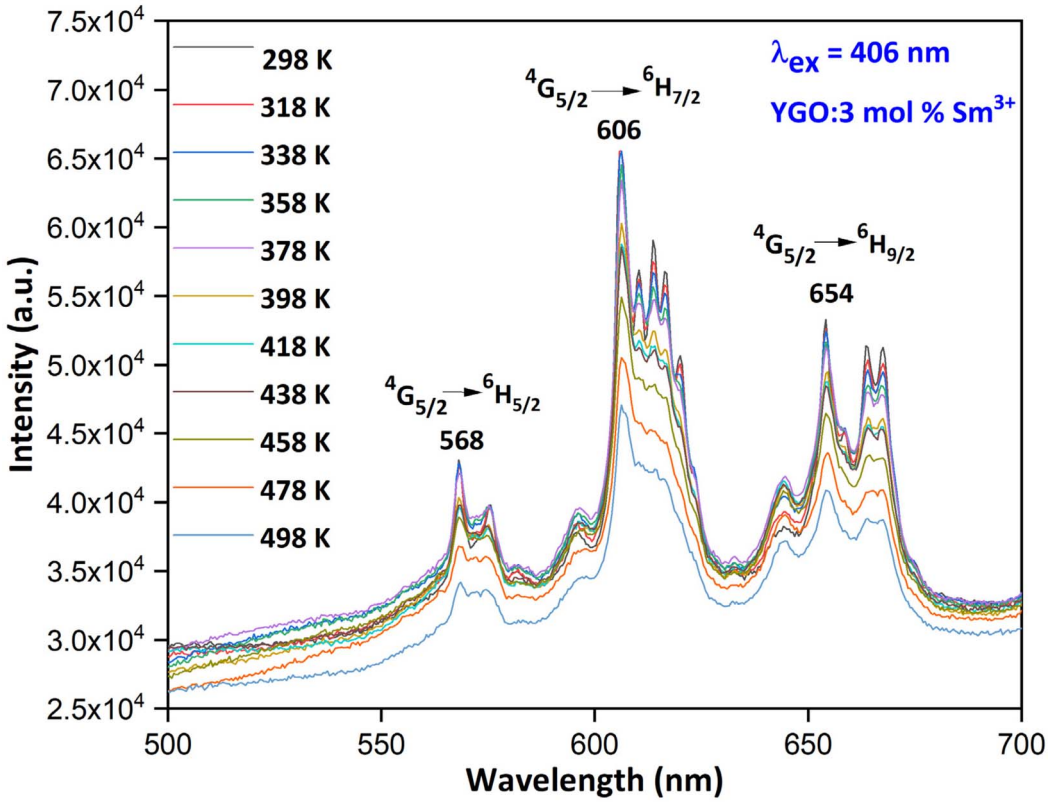

Fig. 16 Temperature-dependent PL spectra of the YGO:3 mol% Sm^{3+} phosphor.

respectively.[59] Hence, to obtain the value of M for Sm^{3+} ions in the host, a plot of $\log(I/x)$ against $\log(x)$ was made, as displayed in Fig. 15, which gives a linear graph with slope $-M/3$. In the current study, the resulting slope is -1.575 and gives $M = 4.725$, which is close to 6, suggesting that dipole–dipole interactions are the ultimate reason for the quenching of Sm^{3+} ions in the lattice.

4.5.5 Temperature-dependent photoluminescence. Thermal stability is an important parameter for confirming the suitability of the synthesized nanophosphor materials for high-power WLED applications. In this study, the thermal stability of the optimized YGO:3 mol% Sm^{3+} nanophosphor was analyzed by taking its PL spectra at varying temperatures under 406 nm excitation, as shown in Fig. 16. The emission pattern of Sm^{3+} ions remained same, but the emission intensity decreased continuously with the rise in temperature from 298 K to 498 K due to the thermal quenching phenomenon. The luminescence intensity was found to retain 71.8% at 473 K compared to its original intensity measured at 298 K (taken to be 100%), confirming that the Sm^{3+} ions in the YGO:3 mol% Sm^{3+} phosphor possess good thermal stability required for high power WLEDs as demonstrated in Fig. 17. Moreover, the activation energy (E_a) serves as an important key factor for determining the thermal stability of a phosphor material. The greater the value of the activation energy, the harder it becomes for activated electrons to overcome the energy barrier. This leads to reduced non-radiative transitions and increased thermal stability of a phosphor. Thus, a higher E_a value means greater luminescence stability. To calculate the value of the activation energy, the Arrhenius model given in eqn (14) may be used[60,61] as follows:

$$I_T = \frac{I_0}{1 + A\exp\left(-\frac{E_a}{k_B T}\right)} \quad (14)$$

This equation can be further modified to become eqn (15) (ref. 62) as follows:

$$\ln\left(\frac{I_0}{I_T} - 1\right) = \ln A - \frac{E_a}{k_B T} \quad (15)$$

In this equation, I_0 and I_T describe luminescence intensities measured at a particular temperature T and at room temperature, respectively. The factor k_B indicates Boltzmann's constant (8.617105×10^{-5} eV K^{-1}), while A represents a constant. The plot of $\ln\left(\frac{I_0}{I_T} - 1\right)$ *versus* $\frac{1}{k_B T}$ is a straight-line graph and the absolute value of the slope gives the activation energy, as displayed in Fig. 18. For the considered nanophosphor, the activation energy was found to be 0.337 eV. The activation energy value and good thermal stability of the optimized YGO:3 mol% Sm^{3+} phosphor indicate that it is a suitable candidate for high-power WLEDs.

4.5.6 Color parameters. Chromaticity coordinates are crucial parameters when analyzing the color output of synthesized phosphors. The CIE 1931 chromaticity triangle developed by the Commission Internationale de l'Eclairage illustrates the

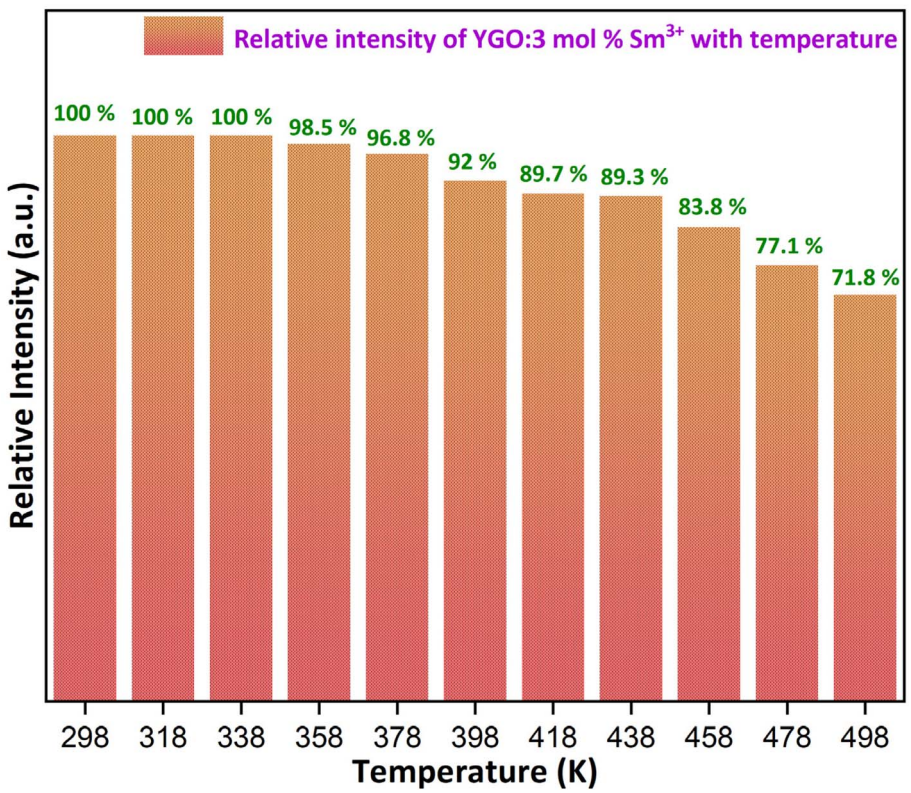

Fig. 17 Bar graph showing the relative intensity of the YGO:3 mol% Sm^{3+} phosphor with temperature.

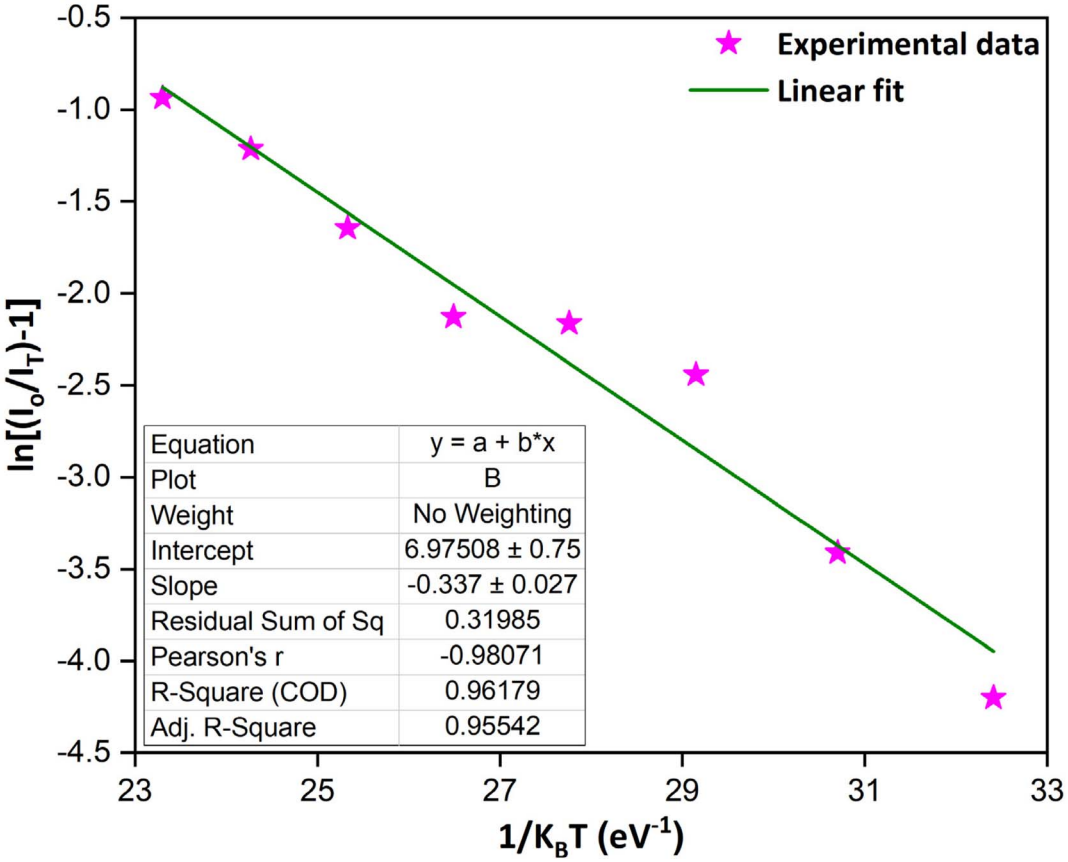

Fig. 18 Linear fitted graph of $\ln[(I_0/I_T) - 1]$ against $1/k_BT$.

spectrum of colors visible to the human eye, using an x–y coordinate framework. The emission color of the produced Y_3GaO_6:Sm^{3+} phosphor samples under 406 nm was evaluated using this color diagram. The obtained PL emission results were analyzed and are depicted in Fig. 19. The determined chromaticity coordinates lie in the orangish region of the spectrum,

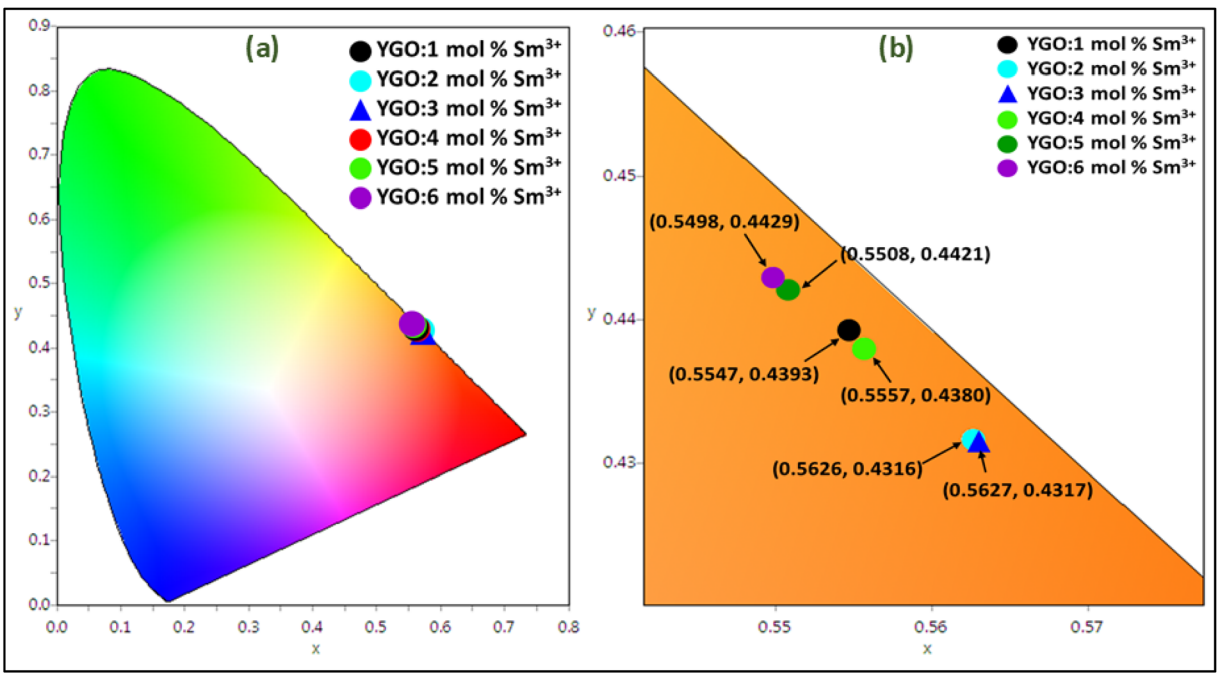

Fig. 19 (a) CIE coordinates (x, y) of the YGO:Sm^{3+} phosphors under 406 nm excitation. (b) Enlarged image of all coordinates.

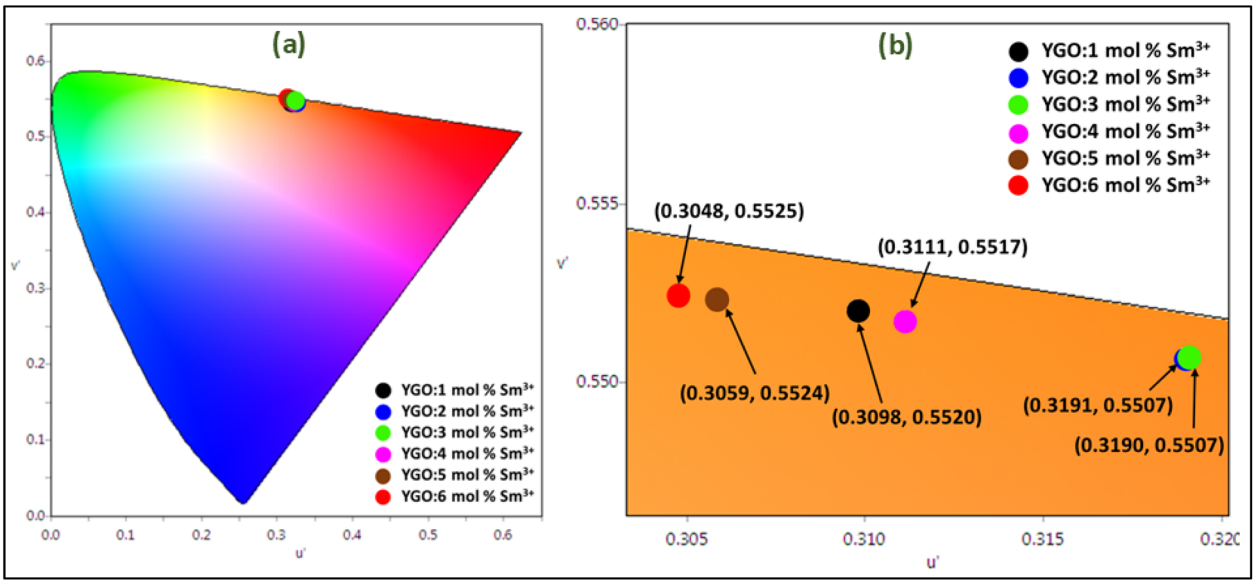

Fig. 20 (a) CIE coordinates (u', v') of the YGO:Sm^{3+} phosphors under 406 nm excitation. (b) Enlarged view of all coordinates.

Table 8 Various color parameters of the $Y_{3-x}GaO_6$:xSm^{3+} (x = 1–6 mol%) phosphors

	CIE coordinates			
Sample	(x, y)	(u', v')	CCT (K)	Color purity (%)
YGO:1 mol% Sm^{3+}	(0.5547, 0.4393)	(0.3098, 0.5520)	1968.83	76.89
YGO:2 mol% Sm^{3+}	(0.5626, 0.4316)	(0.3191, 0.5507)	1885.23	77.81
YGO:3 mol% Sm^{3+}	(0.5627, 0.4317)	(0.3190, 0.5507)	1885.23	78.06
YGO:4 mol% Sm^{3+}	(0.5557, 0.4380)	(0.3111, 0.5517)	1955.89	77.01
YGO:5 mol% Sm^{3+}	(0.5508, 0.4421)	(0.3059, 0.5524)	2008.61	76.27
YGO:6 mol% Sm^{3+}	(0.5498, 0.4429)	(0.3048, 0.5525)	2019.54	76.15

confirming that the synthesized phosphors emit orange-red light on excitation at 406 nm. Using McCamy's relation given in eqn (16), the color temperature (CCT) values for the produced Y_3GaO_6:Sm^{3+} phosphors were also calculated[63] as follows:

$$CCT = -437n^3 + 3601n^2 - 6861n + 5514.31 \quad (16)$$

where $n = \frac{(x - x_e)}{(y - y_e)}$ signifies the inverse slope line, x and y specify the CIE color parameters, and $x_e = 0.332$ and $y_e = 0.186$ designate chroma epicenters. The calculations were made by converting the (x, y) coordinates to (u', v') coordinates (Fig. 20) to analyze CCT values eqn (17) (ref. 64) as follows:

$$u' = \frac{4x}{-2x + 12y + 3}, v' = \frac{9y}{-2x + 12y + 3} \quad (17)$$

The importance of white light can be evaluated by measuring CCT values, which indicate the warmness and coolness of light. For instance, a warm light source has CCT < 3000 K, while a cool light source has CCT > 4000 K. Cool white light is utilized for industrial lighting purposes, while warm white light is used for domestic purposes. The CCT values for all synthesized samples lie in the range 1800–2100 K, demonstrating that the produced light is a warm white light source. Eqn (18) can be used to define the color purity (CP%) of the Y_3GaO_6:Sm^{3+} phosphor samples[65] as follows:

$$CP = \sqrt{\frac{(x - x_i)^2 + (y - y_i)^2}{(x_d - x_i)^2 + (y_d - y_i)^2}} \times 100 \quad (18)$$

Here, (x, y), (x_d, y_d) and (x_i, y_i) denote chromaticity coordinates, dominant and illuminant points, respectively. CIE color coordinates and CCT values, along with the CP of the synthesized phosphor, are briefly listed in Table 8. The observed outcomes of Y_3GaO_6:Sm^{3+} nanophosphors confirm their potential for lighting applications.

5. Conclusions

Sm^{3+}-doped yttrium gallium oxide (Y_3GaO_6) phosphors with different doping concentrations of samarium ions were successfully synthesized using a solution combustion method. To assess their optical behavior, the synthesized samples were subjected to several structural and spectroscopic techniques.

XRD patterns revealed information about the crystalline structure, and Rietveld refinement confirmed the formation of an orthorhombic lattice belonging to the $Cmc2_1$ space group. The surface morphology and elemental composition were examined in detail *via* FE-SEM and EDX studies, respectively. Upon excitation at a wavelength of 406 nm, all Sm^{3+}-incorporated YGO phosphors demonstrated prominent orange photoluminescence at 610 nm, corresponding to the $^4G_{5/2} \rightarrow {}^6H_{7/2}$ transition of Sm^{3+} ions. The bi-exponential behavior of the decay curves is due to the presence of Sm^{3+} ions in two dissimilar crystallographic sites of Y^{3+} ions in the YGO host. The optimal doping level was found to be 3 mol%, yielding the highest emission intensity. Beyond this concentration, a reduction in luminescence was observed due to the concentration quenching effect, attributed to dipole–dipole interactions among Sm^{3+} ions. Chromaticity coordinates derived from photoluminescence spectra positioned in the orange-red portion of the CIE diagram indicate the suitability of these materials for use in lighting applications.

Author contributions

Rinki Jangra: data curation, writing – original draft, investigation, methodology; Devender Singh: writing – review and editing, resources, supervision; Reshu Kajal: validation; Pawan Kumar: project administration; Sitender Singh: formal analysis; Sakshi Wadhwa: visualization; Varun Kumar: software; Harish Kumar: formal analysis; and Ramesh Kumar: visualization.

Conflicts of interest

The authors declare that they have no known competing financial interests or personal relationships that could have appeared to influence the work reported in this paper.

Data availability

Data will be made available upon request.

Acknowledgements

The author Rinki Jangra is thankful to CSIR, New Delhi, India, for providing the financial support under the JRF [09/0382(19584)/2024-EMR-I].

References

1 R. Jangra, D. Singh, R. Kajal, P. Kumar, S. Singh, H. Kumar and R. Kumar, Comprehensive investigation of structural, morphological and optical analysis of Y_3GaO_6:Er^{3+} nanophosphor: A green emitter for white light applications, *J. Mol. Struct.*, 2026, **1369**, 146371, DOI: 10.1016/j.molstruc.2026.146371.

2 H. Kaur, M. Jayasimhadri, M. K. Sahu, P. K. Rao and N. S. Reddy, Synthesis of orange emitting Sm^{3+} doped sodium calcium silicate phosphor by sol-gel method for photonic device applications, *Ceram. Int.*, 2020, **46**, 26434–26439, DOI: 10.1016/j.ceramint.2020.04.224.

3 D. Singh, V. Tanwar, A. P. Simantilleke, B. Mari, P. S. Kadyan and I. Singh, Rapid synthesis and enhancement in down conversion emission properties of $BaAl_2O_4$:Eu^{2+}, RE^{3+} (RE3+= Y, Pr) nanophosphors, *J. Mater. Sci.: Mater. Electron.*, 2016, **27**, 2260–2266, DOI: 10.1007/s10854-015-4020-1.

4 R. T. Maske, A. N. Yerpude, R. S. Wandhare and S. J. Dhoble, Structural, morphological, and photoluminescence properties of RE (RE= Dy^{3+}, Eu^{3+}, Sm^{3+}) -doped $CaAlBO_4$ phosphor synthesized by combustion method, *Luminescence*, 2023, **38**, 1814–1824, DOI: 10.1002/bio.4568.

5 S. Singh, P. Kumar, I. Gupta, P. Siwach and D. Singh, Persistent luminescence in comparison to phosphorescence, In *Persistent Luminescence: Fundamentals, Mechanisms and Applications*, Springer Nature Singapore, Singapore, 2024, pp. 1–45, DOI: 10.1007/978-981-97-4943-0_1.

6 B. Marí, K. C. Singh, P. Cembrero-Coca, I. Singh, D. Singh and S. Chand, Red emitting $MTiO_3$ (M= Ca or Sr) phosphors doped with Eu^{3+} or Pr^{3+} with some cations as co-dopants, *Displays*, 2013, **34**, 346–351, DOI: 10.1016/j.displa.2013.07.003.

7 K. B. Morebodi, L. Reddy, M. L. Letswalo, A. Balakrishna, L. J. Erasmus, H. C. Swart and P. L. Masiteng, Synthesis and investigation of energy transfer mechanism in Sm^{3+} and Eu^{3+} doped $Na_6Mg(SO_4)_4$ nanophosphors via solution combustion technique, *Inorg. Nano-Met. Chem.*, 2024, **54**, 1026–1037, DOI: 10.1080/24701556.2022.2081196.

8 D. Singh, S. Sheoran, V. Tanwar and S. Bhagwan, Optical characteristics of Eu (III) doped $MSiO_3$ (M= Mg, Ca, Sr and Ba) nanomaterials for white light emitting applications, *J. Mater. Sci. Mater. Electron.*, 2017, **28**, 3243–3253, DOI: 10.1007/s10854-016-5914-2.

9 V. Singh, S. Kumari, M. M. Haidari, A. A. Bhat, A. S. Rao and J. B. Joo, Photoluminescence Behavior of Sm^{3+}-Doped YPO_4 Phosphors for Solid-State Lighting, *Luminescence*, 2025, **40**, e70190, DOI: 10.1002/bio.70190.

10 D. Singh, V. Tanwar, A. P. Samantilleke, B. Mari, S. Bhagwan, P. S. Kadyan and I. Singh, Preparation and photoluminescence properties of $SrAl_2O_4$:Eu^{2+}, RE^{3+} green nanophosphors for display device applications, *J. Electron. Mater.*, 2016, **45**, 2718–2724, DOI: 10.1007/s11664-015-4318-z.

11 M. K. Pradhan and S. Dash, Insights into structural and spectroscopic characterization of Sm^{3+} doped orange rich red emitting $CsMgPO_4$ phosphors, *J. Rare Earths*, 2022, **40**, 1837–1848, DOI: 10.1016/j.jre.2022.01.014.

12 R. Kajal, D. Singh, R. Jangra, P. Kumar, R. Kumar and H. Kumar, Insights into reddish-orange emitting Gd_3GaO_6:Sm^{3+} phosphor: Structural refinement and photoluminescence characteristics for warm white LEDs, *Opt. Mater.*, 2026, **176**, 118095, DOI: 10.1016/j.optmat.2026.118095.

13 K. Su, Q. Zhang, X. Yang and B. Ma, Crystal structure and luminescence properties of thermally stable Sm^{3+}-doped

$Sr_9In(PO_4)_7$ orange-red phosphor, *J. Phys. D: Appl. Phys.*, 2020, **53**, 385101, DOI: 10.1088/1361-6463/ab938d.

14 R. Jangra, D. Singh, R. Kajal, P. Kumar, H. Kumar and R. Kumar, Structural refinement, Judd-Ofelt parameters and optoelectronic properties of Eu^{3+} doped Y_3GaO_6 phosphor: An efficient red emitter for WLEDs, *Ceram. Int.*, 2026, **52**, 19037–19047, DOI: 10.1016/j.ceramint.2026.03.002.

15 R. Cao, Y. Ren, T. Chen, W. Wang, Q. Guo, Q. Hu, C. Liao and T. Fan, Emission improvement and tunable emission properties of $SrZrSi_2O_7$:R (R= Sm^{3+} and Sm^{3+}/Bi^{3+}) phosphors, *J. Lumin.*, 2020, **225**, 117350, DOI: 10.1016/j.jlumin.2020.117350.

16 P. Kumar, S. Singh, I. Gupta, V. Kumar and D. Singh, Luminous $LaAlO_3:Dy^{3+}$ perovskite nanomaterials: Synthesis, structural, and luminescence characteristics for white light-emitting diodes, *Luminescence*, 2022, **37**, 1932–1941, DOI: 10.1002/bio.4377.

17 R. Cao, M. Wu, B. Lan, T. Huang, J. Nie, F. Cheng, X. Luo and J. Wang, Study on the properties of Sm^{3+}-Doped $CaTbAl_3O_7$ phosphors, *J. Lumin.*, 2025, **277**, 120898, DOI: 10.1016/j.jlumin.2024.120898.

18 I. Gupta, S. Singh, S. Bhagwan and D. Singh, Rare earth (RE) doped phosphors and their emerging applications: A review, *Ceram. Int.*, 2021, **47**, 19282–19303, DOI: 10.1016/j.ceramint.2021.03.308.

19 P. Kumar, D. Singh, I. Gupta, S. Singh, S. Nehra and R. Kumar, Realization of warm reddish-orange light emitter single phase $Y_4Al_2O_9:Sm^{3+}$ nanophosphors for indoor lighting applications, *J. Lumin.*, 2023, **257**, 119703, DOI: 10.1016/j.jlumin.2023.119703.

20 D. Espinoza, N. L. Allan, R. Castillo, S. Conejeros, I. Brito, I. R. Martin, P. Alemany and J. Llanos, Energy transfer, structural and luminescent properties of the color tunable phosphor $Y_2WO_6:Sm^{3+}$, *J. Alloys Compd.*, 2020, **835**, 155381, DOI: 10.1016/j.jallcom.2020.155381.

21 R. Kajal, D. Singh, R. Jangra, P. Kumar, V. Kumar, H. Kumar and R. Kumar, Structural and photophysical investigation of gadolinium based Eu^{3+} doped Gd_3GaO_6 phosphor: A red emitter with high color purity for WLEDs application, *J. Alloys Compd.*, 2025, **1050**, 185688, DOI: 10.1016/j.jallcom.2025.185688.

22 S. Singh, D. Singh, P. Siwach, I. Gupta and P. Kumar, Synthesis strategies for rare earth activated inorganic phosphors: a mini review, *Appl. Res.*, 2025, **4**, e202400190, DOI: 10.1002/appl.202400190.

23 X. Peng, X. Guo, R. Cui, P. Ling-hu, J. Zhang and C. Deng, Novel orange red phosphor $BaLaGaO_4:Sm^{3+}$ with high quantum efficiency and good thermal stability for indoor illumination and anti-counterfeiting inks applications, *Ceram. Int.*, 2024, **50**, 30111–30123, DOI: 10.1016/j.ceramint.2024.05.310.

24 V. Govindan, A. Raja, G. M. Das, R. Dwivedi, I. Kindrat and D. J. Daniel, Structural, optical, elemental and photometric properties of Sm^{3+} activated $Ca_3Ga_4O_9$ oxide phosphors for WLEDs, *Colloids Surf. A Physicochem. Eng. Asp.*, 2023, **675**, 131973, DOI: 10.1016/j.colsurfa.2023.131973.

25 C. A. Kodaira, R. Stefani, A. S. Maia, M. C. Felinto and H. F. Brito, Optical investigation of Y{sub 2}O{sub 3}:Sm {sup 3+} nanophosphor prepared by combustion and Pechini methods, *J. Lumin.*, 2007, **127**, 616–622, DOI: 10.1016/j.jlumin.2007.03.016.

26 R. Kajal, R. Jangra, P. Kumar, D. Singh, R. Kumar and H. Kumar, Structural, morphological and optical characteristics of Er^{3+} doped Gd_3GaO_6 phosphor for efficient green emission in solid state lighting, *J. Mol. Struct.*, 2026, **1359**, 145495, DOI: 10.1016/j.molstruc.2026.145495.

27 D. Navami, R. B. Basavaraj, G. P. Darshan, H. K. Inamdar, S. C. Sharma, H. B. Premkumar and H. Nagabhushana, Evolution of shapes and identification of level II and III features of fingerprints using $CaZrO_3:Sm^{3+}$ fluorescent markers prepared via solution combustion route, *Opt. Mater.*, 2019, **88**, 479–487, DOI: 10.1016/j.optmat.2018.11.058.

28 S. Singh and D. Singh, Structural and optical properties of green emitting $Y_2SiO_5:Tb^{3+}$ and $Gd_2SiO_5:Tb^{3+}$ nanoparticles for modern lighting applications, *Rare Met.*, 2021, **40**, 3289–3298, DOI: 10.1007/s12598-020-01585-0.

29 T. S. Dhapodkar, A. R. Kadam and S. J. Dhoble, Combustion-assisted $Ca_{8.25}Na_{1.5}Al_6O_{18}:Sm^{3+}$ phosphors for solid-state lighting and WLED applications, *Luminescence*, 2022, **37**, 1899–1905, DOI: 10.1002/bio.4371.

30 D. Singh, V. Tanwar, S. Bhagwan, P. S. Kadyan and B. Mari, Synthesis and Luminescent Characterization of $MAlO_3:Eu^{3+}$ Red Nanophosphors, *Adv. Sci. Lett.*, 2014, **20**, 1726–1729, DOI: 10.1166/asl.2014.5736.

31 Q. Sun, Y. Du, X. Wu, W. Liu, L. Li, H. Li, J. Zhao and G. Rao, Intense and sensitive green mechanoluminescence by Tb^{3+} doping in Y_3GaO_6, *Ceram. Int.*, 2024, **50**, 44417–44425, DOI: 10.1016/j.ceramint.2024.08.289.

32 F. Chi, Y. Zheng, J. Zhang, X. Niu, J. Liu, S. Liu, X. Zhang, B. Jiang and X. Wei, Tb^{3+}/Eu^{3+} doped Y_3GaO_6 phosphors for color tunable emission, *Ceram. Int.*, 2025, **51**, 37443–37451, DOI: 10.1016/j.ceramint.2025.05.450.

33 R. Kajal, D. Singh, R. Jangra, B. Dahiya, M. Kadian, P. Kumar, R. Kumar and H. Kumar, Orthorhombic $Gd_3GaO_6:Dy^{3+}$ nanophosphors with tunable luminescence: Structural, morphological and photometric insights for WLEDs, *Opt. Mater.*, 2026, **174**, 117942, DOI: 10.1016/j.optmat.2026.117942.

34 P. Kumar, D. Singh, S. Kadyan, H. Kumar and R. Kumar, Insights into opto-electronic investigation of highly pure reddish-orange light emissive Sm^{3+} doped $Y_2Si_2O_7$ phosphors: tailored for NUV-excitable white light emitting diodes, *J. Mol. Struct.*, 2024, **1314**, 138727, DOI: 10.1016/j.molstruc.2024.138727.

35 I. Gupta, D. Singh, S. Singh, P. Kumar, S. Bhagwan and V. Kumar, Study of structural and spectroscopic characteristics of novel color tunable yellowish-white Dy^{3+} doped $Gd_4Al_2O_9$ nanophosphors for NUV-based WLEDs, *J. Mol. Struct.*, 2023, **1272**, 134199, DOI: 10.1016/j.molstruc.2022.134199.

36 D. Singh, V. Tanwar, A. P. Simantilleke, S. Bhagwan, B. Mari, P. S. Kadyan, K. C. Singh and I. Singh, Synthesis and enhanced luminescent characterization of $SrAl_4O_7:Eu^{2+}$, RE^{3+} (RE = Nd, Dy) nanophosphors for light emitting applications, *J. Mater. Sci.: Mater. Electron.*, 2016, **27**, 5303–5308, DOI: 10.1007/s10854-016-4428-2.

37 P. Kumar, S. Singh, I. Gupta, V. Kumar and D. Singh, Structural and optical characterization of trivalent samarium-activated $LaAlO_3$ nanocrystalline materials for solid-state lighting, *J. Mol. Struct.*, 2022, **1265**, 133362, DOI: 10.1016/j.molstruc.2022.133362.

38 P. Kumar, D. Singh, I. Gupta, S. Singh, S. Nehra and R. Kumar, A study of phase evolution, crystallographic and down-conversion luminescent behaviour of monoclinic $Y_4Al_2O_9:Dy^{3+}$ nanophosphors for white light applications, *Opt. Mater.*, 2023, **138**, 113677, DOI: 10.1016/j.optmat.2023.113677.

39 I. Gupta, P. Kumar, S. Singh, S. Bhagwan, S. K. Chhikara and D. Singh, Crystal configuration, spectroscopic and optical characteristics of Er^{3+} doped $YAlO_3$ perovskites for advanced photonic appliances, *Inorg. Chim. Acta.*, 2022, **543**, 121183, DOI: 10.1016/j.ica.2022.121183.

40 H. R. Shih and Y. S. Chang, Structure and photoluminescence properties of Sm^{3+} ion-doped $YInGe_2O_7$ phosphor, *Materials*, 2017, **10**, 779, DOI: 10.3390/ma10070779.

41 A. Dalal, K. Nehra, A. Hooda, S. Bhagwan, R. K. Saini, D. Singh and S. Kumar, Luminescent heteroleptic samarium (III) complexes: synthesis, optical and photophysical investigation, *Inorg. Chem. Commun.*, 2022, **141**, 109620, DOI: 10.1016/j.inoche.2022.109620.

42 D. Rani, A. Kumar, M. Dahiya, M. Malik and D. Kumar, Highly efficient red emission from novel Sm^{3+} doped $Na_3La(PO_4)_2$ nanophosphors for optoelectronic applications, *J. Fluoresc.*, 2025, **35**, 5105–5117, DOI: 10.1007/s10895-024-03876-6.

43 I. Gupta, S. Singh, P. Kumar, S. Bhagwan, V. Tanwar, S. Nehra, V. Kumar and D. Singh, Synthetic, structural and optical characteristic of novel color tunable reddish-orange $Gd_4Al_2O_9:Sm^{3+}$ nanocrystalline materials for solid-state photonic appliances, *Inorg. Chem. Commun.*, 2023, **148**, 110332, DOI: 10.1016/j.inoche.2022.110332.

44 D. R. Taikar, S. Tamboli and S. J. Dhoble, Synthesis and photoluminescence properties of red, green and blue emitting $LaYO_3$:M (M= Eu^{3+}, Tb^{3+}, Sm^{3+}, Bi^{3+}, Pb^{2+}) phosphors, *Optik*, 2017, **142**, 183–190, DOI: 10.1016/j.ijleo.2017.05.095.

45 I. Gupta, P. Kumar, S. Singh, S. Bhagwan, V. Kumar and D. Singh, Phase recognition, structural measurements and photoluminescence studies of reddish-orange-emissive $YAlO_3:Sm^{3+}$ perovskite nanophosphors for NUV energized WLEDs, *J. Mol. Struct.*, 2022, **1267**, 133567, DOI: 10.1016/j.molstruc.2022.133567.

46 H. R. Shih and Y. S. Chang, Structure and photoluminescence properties of Sm^{3+} ion-doped $YInGe_2O_7$ phosphor, *Materials*, 2017, **10**, 779, DOI: 10.3390/ma10070779.

47 P. Kumar, D. Singh and H. Kumar, Orangish-red light emitting $LaSr_2AlO_5:Sm^{3+}$ nanophosphors for warm LEDs: Crystallographic, photoluminescence characteristics with high color purity and thermal stability, *Mater. Chem. Phys.*, 2014, **320**, 129418, DOI: 10.1016/j.matchemphys.2024.129418.

48 F. B. Xiong, F. X. Xu, H. F. Lin, Y. P. Wang, E. Ma and W. Z. Zhu, Synthesis and luminescent properties of novel thermal-stable orangish-red-emitting $LnNbO4:Sm^{3+}$ (Ln= La, Y) phosphors, *Appl. Phys. A*, 2020, **126**, 908, DOI: 10.1007/s00339-020-04090-4.

49 D. Singh and S. Sheoran, Synthesis and luminescent characteristics of $M_3Y_2Si_3O_{12}:Eu^{3+}$ (M= Ca, Mg, Sr and Ba) nanomaterials for display applications, *J. Mater. Sci.: Mater. Electron.*, 2016, **27**, 12707–12718, DOI: 10.1007/s10854-016-5405-5.

50 R. Nagaraj, A. Raja and S. Ranjith, Synthesis and luminescence properties of novel red-emitting Eu^{3+} ions doped silicate phosphors for photonic applications, *J. Alloys Compd.*, 2020, **827**, 154289, DOI: 10.1016/j.jallcom.2020.154289.

51 I. Gupta, D. Singh, S. Singh, P. Kumar, S. Bhagwan and V. Kumar, Phase recognition and spectroscopic characteristics of single-phase Tb^{3+} doped $Gd_4Al_2O_9$ nanophosphors for NUV energized advanced photonic appliances, *J. Lumin.*, 2022, **252**, 119327, DOI: 10.1016/j.jlumin.2022.119327.

52 M. Malik and D. Kumar, Synthesis and optical evaluation of Dy^{3+} doped $CaGdAl_3O_7$ nanophosphor for cool white light emission, *J. Mater. Sci.: Mater. Electron.*, 2025, **36**, 1243, DOI: 10.1007/s10854-025-15217-9.

53 P. Kumar, S. Singh, I. Gupta, A. Dalal, V. Kumar and D. Singh, Preparation, structural and photometric properties of single-phased $Gd_3Al_5O_{12}:Tb^{3+}$ green-emitting phosphors for solid state lighting purpose, *Mater. Sci. Eng.: B*, 2023, **288**, 116189, DOI: 10.1016/j.mseb.2022.116189.

54 F. Yang, Y. Liu, X. Tian, G. Dong and Q. Yu, Luminescence properties of phosphate phosphor $Ba_3Y(PO_4)_3:Sm^{3+}$, *J. Solid State Chem.*, 2015, **225**, 19–23, DOI: 10.1016/j.jssc.2014.11.025.

55 I. Gupta, D. Singh, P. Kumar, S. Singh, S. Bhagwan and V. Kumar, Structural, morphological, and optical characteristics of $Gd_2Si_2O_7:Dy^{3+}$ nanophosphors for WLEDs, *Luminescence*, 2023, **38**, 1789–1802, DOI: 10.1002/bio.4566.

56 N. R. Srinath, H. C. Manjunatha, Y. S. Vidya, R. Ramaraghavulu, S. R. Farheen, R. Munirathnam, K. N. Sridhar, S. Manjunatha, M. Shivanna and S. Kumar, Effect of Sm^{3+} concentration on reddish orange photoluminescence and electrochemical properties of copper aluminate nanoparticles for display and supercapacitor applications, *Microchem. J.*, 2024, **205**, 111151, DOI: 10.1016/j.microc.2024.111151.

57 I. Gupta, D. Singh, S. Singh, P. Kumar, S. Bhagwan and V. Kumar, Structural and photophysical measurements of Er^{3+} doped $Gd_4Al_2O_9$ nanophosphors for NUV excitable

solid-state lighting applications, *Chem. Phys. Lett.*, 2023, **814**, 140350, DOI: 10.1016/j.cplett.2023.140350.

58 I. Kumar and A. K. Gathania, Photoluminescence and quenching study of the Sm^{3+}-doped $LiBaPO_4$ phosphor, *J. Mater. Sci.: Mater. Electron.*, 2022, **33**, 328–341, DOI: 10.1007/s10854-021-07301-7.

59 I. Gupta, D. Singh, S. Singh, P. Kumar, S. Bhagwan, V. Kumar, H. Kumar and S. K. Chhikara, Crystallographic, morphological and photoluminescent investigations of Tb^{3+}-doped $YAlO_3$ perovskites for lighting applications, *Luminescence*, 2023, **38**, 585–599, DOI: 10.1002/bio.4486.

60 T. Lu, Z. Ma, C. Du, Y. Fang, H. Wu, Y. Jiang, L. Wang, L. Dai, H. Jia, W. Liu and H. Chen, Temperature-dependent photoluminescence in light-emitting diodes, *Sci. Rep.*, 2014, **4**, 6131, DOI: 10.1038/srep06131.

61 R. Jangra, D. Singh, R. Kajal, B. Dahiya, E. Poonia, P. Kumar, V. Kumar, H. Kumar and R. Kumar, Combustion based orthorhombic Y_3GaO_6:Dy^{3+} phosphor: Structural stability, morphology and luminescence studies for optoelectronic applications, *Inorg. Chem. Commun.*, 2026, **187**, 116405, DOI: 10.1016/j.inoche.2026.116405.

62 R. Kajal, D. Singh, R. Jangra, P. Kumar, V. Kumar, R. Kumar and H. Kumar, Synthesis, structural refinement and luminescence properties of green-emitting Gd_3GaO_6:Tb^{3+} phosphors for display applications, *RSC Adv.*, 2026, **16**, 10720–10734, DOI: 10.1039/D5RA07419C.

63 A. Hooda, A. Dalal, K. Nehra, P. Kumar, D. Singh, R. S. Malik and S. Kumar, Heteroleptic Eu (III) emissive complexes: Luminescent, optoelectronic and theoretical investigation, *J. Lumin.*, 2022, **252**, 119272, DOI: 10.1016/j.jlumin.2022.119272.

64 P. Kumar, D. Singh, I. Gupta, S. Singh, V. Kumar, H. Kumar and S. K. Chhikara, Cool green light emitting $GdAlO_3$:Tb^{3+} perovskite nanomaterials: Crystal structure and spectroscopic characteristics for advance display appliances, *Inorg. Chem. Commun.*, 2022, **145**, 110064, DOI: 10.1016/j.inoche.2022.110064.

65 S. Ling, F. B. Xiong, W. B. Yang, H. F. Lin and W. Z. Zhu, Novel Sm^{3+}/Eu^{3+} co-doped $Sr_7Sb_2O_{12}$ red-emitting phosphor for white LED, *Inorg. Chem. Commun.*, 2023, **150**, 110365, DOI: 10.1016/j.inoche.2022.110365.